Interfaces in Garnet-Based All-Solid-State Lithium Batteries

Dawei Wang, Changbao Zhu,* Yanpeng Fu, Xueliang Sun,* and Yong Yang*

All-solid-state lithium batteries (ASSLBs) are considered to be the next-generation energy storage system, because of their overwhelming advantages in energy density and safety compared to conventional lithium ion batteries. Among various systems, garnet-based ASSLBs are one of the most promising candidates. The advantages arise from the intrinsic properties of garnet electrolytes, especially the high shear modulus and wider electrochemical window compared to that of polymer and sulfide electrolytes, guaranteeing the application of Li metal and high voltage cathodes. However, the interfacial issues between garnets and electrodes (Li metal and cathodes) are challenging and hinder the further development of garnet-based ASSLBs. Herein, the origin of interfacial resistance and recent development of interfacial construction in garnet-based ASSLBs are reviewed, as well as the subsequent interfacial degradation and cell failure during cycling process, including inhomogeneous plating and stripping, Li dendrites, and strain induced microcracks in stiff electrodes. Finally, the future challenges and opportunities in this important and exciting field are also presented.

1. Introduction

All-solid-state lithium batteries (ASSLBs) are promising candidates to replace conventional lithium ion batteries (LIBs). LIBs have dominated the market ranging from portable electronics to electric cars, however, they still suffer with safety issues, expensive sealing agent, and catastrophic failure caused by organic liquid electrolytes. ASSLBs exhibit overwhelming advantages as follows: 1) No electrolyte leakage. The most obvious advantage of ASSLBs is the avoidance of electrolyte leakage, and related issues such as fire hazard, electrical short circuit and corruption. In addition, ASSLBs do not need advance sealants, pressurizing electrolyte, and flame retardant failsafe.[1,2] 2) No thermal runaway. Thermal runaway will cause the rise of internal temperature, pressure, and vent of flammable gases in conventional LIBs, at a risk of explosion and shrapnel.[3,4] ASSLBs avoid the use of organic electrolytes and prevent the thermal runaway for a large extent.[5] 3) High resistance to lithium dendrite. The lithium dendrite may form during deposition process and penetrate through the separator, potentially cause a short circuit in conventional LIBs.[6] ASSLBs using solid electrolytes (SEs) with high shear modulus are expected to prevent/alleviate the dendrite penetration and extend the cell life. 4) Higher energy density.[7] The conventional LIBs are not suitable for the application of high voltage cathode and lithium metal anode because of narrow electrochemical window of liquid electrolytes, as well as failure in preventing lithium dendrite. ASSLBs facilitate the application of high voltage cathode materials and high energy density lithium metal anode, therefore increasing the energy density of the whole cell.

Figure 1 shows the scheme of a typical ASSLB. Similar with conventional LIBs, the main components of ASSLB are cathode, SE, and anode. The distinctive component is SE, and its properties support the great advantages of ASSLBs. These properties include stability at ultrahigh and ultralow temperature, high mechanical strength,[8] wider electrochemical window (with passivation), and so on.[9–11] According to the category of SE, ASSLBs are divided into polymer-based, oxide-based, and sulfide-based systems, corresponding to the polymer, oxide, and sulfide electrolytes, respectively. Therein, oxide electrolytes exhibit moderate ionic conductivity, high shear modulus, and better stability with atmosphere and electrodes, are promising candidates for ASSLB. Specifically, oxide electrolytes are classified into LISICON ($Li_{14}ZnGe_4O_{16}$), NASICION ($LiTi_2(PO_4)_3$), perovskite ($Li_{3x}La_{0.67−x}\Box_{0.33−2x}TiO_3$), garnet ($Li_{3.7}LnMO_{12}$, Ln = Y, Pr, Nd, La, Sm–Lu, M = Zr, Sb, W, etc.), and so on based on their structure. Without reductive Ge, Ti elements in the composition, garnets are normally considered most promising among oxide electrolytes.[12,13]

Garnet-type electrolytes in the formula of $Li_{3.7}Ln_3M_2O_{12}$, show a space group $Ia\bar{3}d$. Lithium content ranges from 3 to 7 based on the substitution elements at Ln and M sites.[14,15]

Dr. D. Wang, Prof. C. Zhu
Department of Materials Science and Engineering
Sun Yet-sen University
Guangzhou, Guangdong 510275, China
E-mail: zhuchb6@mail.sysu.edu.cn
Dr. D. Wang, Prof. X. Sun
Department of Mechanical and Materials Engineering
University of Western Ontario
1151 Richmond St, London, Ontario N6A 3K7, Canada
E-mail: xsun9@uwo.ca
Dr. Y. Fu
School of Materials and Energy
Guangdong University of Technology
Guangzhou, Guangdong 510006, China
Prof. Y. Yang
Collaborative Innovation Center of Chemistry for Energy Materials
State Key Laboratory Physical Chemistry Solid Surfaces
Department of Chemistry
Xiamen University
Xiamen, Fujian 361005, China
E-mail: yyang@xmu.edu.cn

ADVANCED
SCIENCE NEWS
www.advancedsciencenews.com

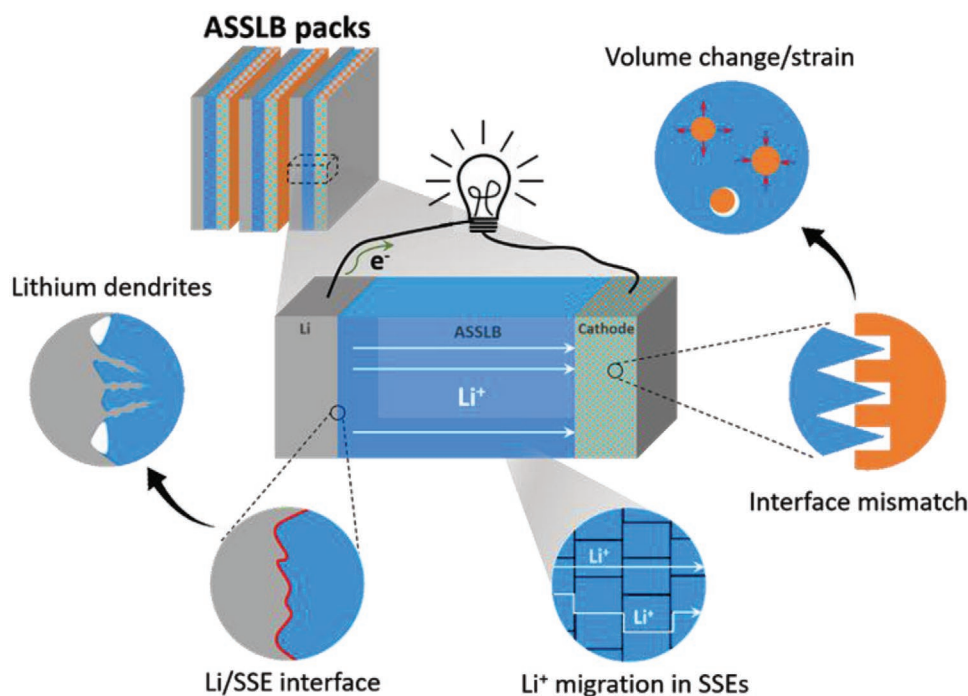ADVANCED
ENERGY
MATERIALS
www.advenergymat.de

Figure 1. Scheme of all-solid-state lithium batteries (ASSLBs). Showing the components and challenges in ASSLBs, including solid electrolyte (SE), interfaces between SE and Li metal, SE and cathode materials, and their degradation during charge–discharge process.

Normally, garnets are classified into Li3 ($Li_3Ln_3Te_2O_{12}$; Ln = Y, Pr, Nd, Sm–Lu),[16–18] Li5 ($Li_5La_3M_2O_{12}$; M = Nb, Ta, Sb),[19] and Li7 ($Li_7La_3M_2O_{12}$; M = Zr, Sn, Hf) categories,[20–23] according to the Li content in the formula. Li3 system shows a typical garnet structure, Li occupies tetrahedral 24d sites, Ln occupies 24c sites, M occupies 16a sites, and O occupies 96h site. Li5 and Li7 systems are called Li-stuffed structure, and the extra Li occupies octahedral 48g and distorted 96h sites. With the increase of Li content from 3 to 7, more Li occupies active octahedral 48g and 96h sites rather than inactive 24d sites, and the Li^+ conductivity increases correspondingly. State-of-the-art, the ionic conductivity of garnets is on the order of $10^{-3}–10^{-4}$ S cm^{-1}, which is satisfied for ASSLBs. Fundamentally, Li^+ transports along 24d-96h-48g-96h-24d route in Li7 structure. Therein, the tetrahedral 24d sites as the key points in the route, determine the bulk conductivity.[24–26] Therefore, any strategies tuning the Li^+ concentration and Li^+ dynamics at 24 sites, can improve the ionic conductivity. In addition, although garnets exhibit a better stability with environment than other electrolytes, slight side reactions still happen at the surface, typically examples are the formation of Li_2CO_3 and LiOH due to Li^+/H^+ exchange between garnet and moisture.[27–31] The detailed properties of garnet electrolytes were summarized in several reviews, and will not be specified here.[32–35]

However, the interfacial construction between garnets and electrodes (lithium metal and cathode materials) is challenging, which hampers the further development of garnet-based ASSLBs.[36] Moreover, even excellent interfaces are initially built, the interfacial degradation is likely to occur during charge–discharge process, such as inhomogeneous stripping and plating of lithium metal, volume change induced mechanical separation in stiff cathode materials. Although there are

several reviews related to the interfacial issues in ASSLBs, the specific discussion of interfacial problems for garnet-based ASSLBs is deficient.[37–43]

Herein, we reviewed the origin of interfacial resistance, strategies of reducing the interfacial resistance and interface evolution during cycling process for both anodic and cathodic interfaces, in order to shed light on interfacial construction in garnet-based ASSLBs.

2. Lithium/Garnet Interface

Lithium metal is expected as an ideal anode because of its high specific capacity (3860 mAh g^{-1}) and low electrochemical potential (−3.04 V vs standard hydrogen electrode). However, this low electrochemical potential makes lithium unstable with most of the electrolytes. In addition, lithium dendrites seriously occur in lithium metal batteries, resulting in safety issues. Garnet electrolytes with wider electrochemical window (with passivation) and higher shear modulus, are promising in revival of lithium metal anode, thereby enhancing the energy density of ASSLBs.[44] Nevertheless, achieving fast interfacial kinetics, remaining interfacial stability and avoiding lithium dendrites during cycling are still challenging in the applications.

2.1. Chemical Stability with Lithium Metal Anode

Chemical stability with lithium metal needs special attention when choosing an SE for ASSLBs. Three types of Li/SE interface were classified by Wenzel et al.[45] a) Thermodynamically stable interface. In this case, SEs are absolutely stable
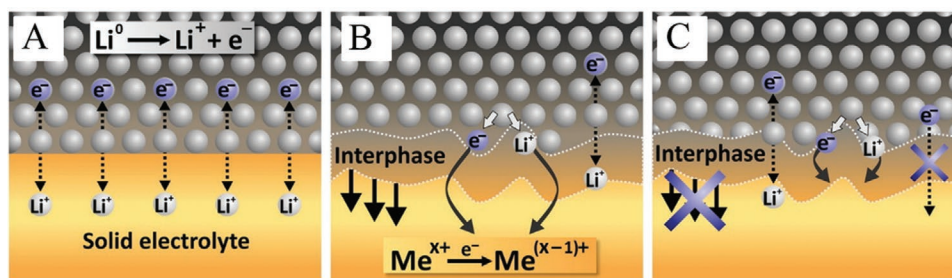
Figure 2. Interfaces between lithium metal and SE. A) Thermodynamically stable interface. B) Reactive and mixed conducting interphase. C) Reactive and metastable solid-electrolyte interphase. Reproduced with permission.[45] Copyright 2015, Elsevier B.V.

with lithium metal, forming a sharp and clear 2D interface (**Figure 2**A). b) The second case is thermodynamically unstable interface, and chemical reaction occurs between SEs and lithium metal. If the newly formed interphases are partially electronically conductive, chemical reaction propagates into SEs, thereby reducing the bulk materials gradually. Once the SE is completely reduced and becomes a mixed conductor, short circuit happens (Figure 2B). c) In contrast to the second case, if the reaction products are electronically insulative or the electronic conductivity is low enough to limit the growth of the interphase, a stable 3D thin interface can be formed (Figure 2C).

Garnet-type electrolytes are firstly considered stable with lithium metal, judging from the changeless outward color when contacted with solid or molten Li foil.[46–49] However, judging from the color is limited because of its low sensitivity. Thereafter, high surface sensitive techniques were undertaken in order to characterize the chemical stability of Li metal with garnets. The results showed that the garnets are not absolutely stable with Li metal, and the side reactions are dependent on the garnet composition. Fingerle et al. applied X-ray and ultraviolet photoelectron spectroscopy to study the stability of $Li_5La_3Ta_2O_{12}$ against Li after thermal deposition (**Figure 3**A).[50] Upon thermal treatment, the structure of $Li_5La_3Ta_2O_{12}$

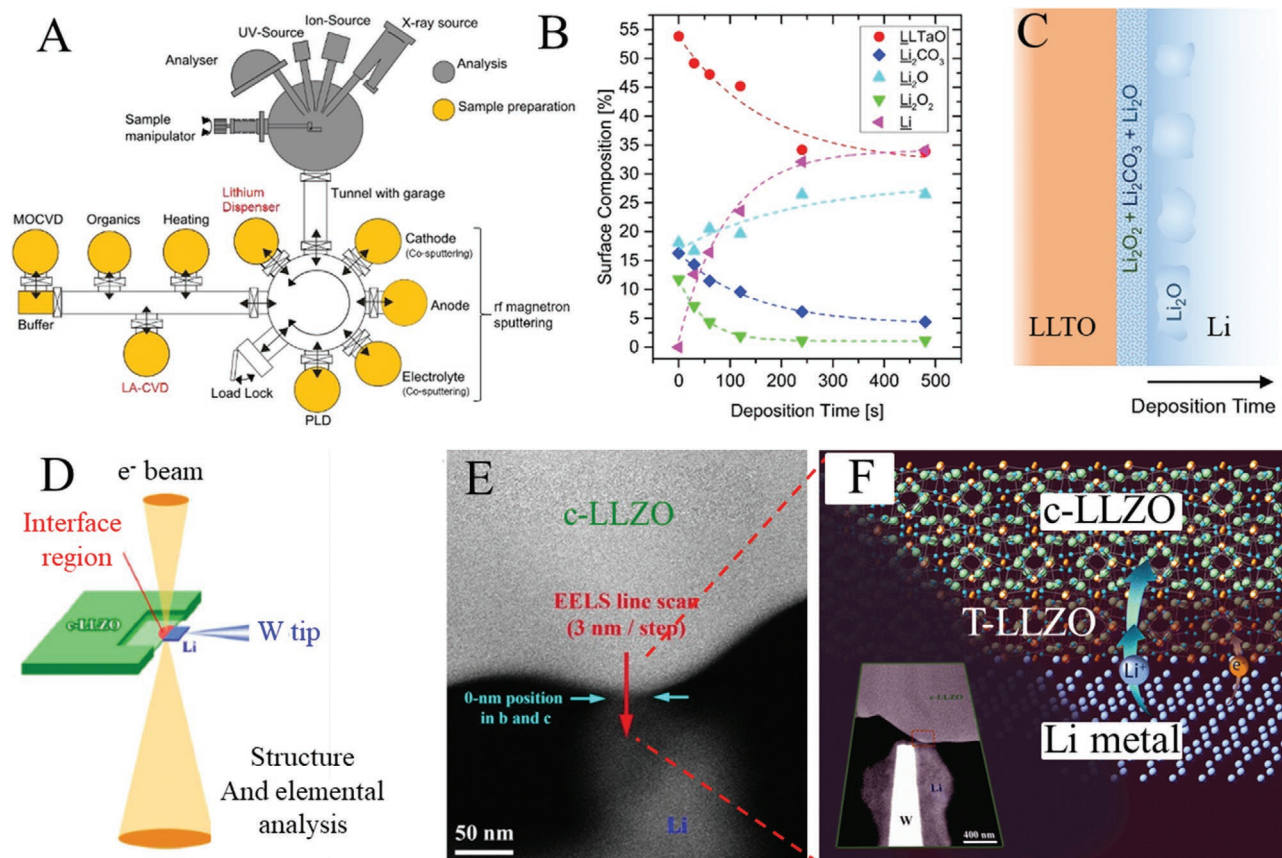**Figure 3.** A–C) X-ray and ultraviolet photoelectron spectroscopy characterization of $Li_5La_3Ta_2O_{12}$ against Li. Reproduced with permission.[50] Copyright 2017, Elsevier B.V. D–F) Scanning transmission electron spectroscopy characterization of $Li_7La_3Zr_2O_{12}$ with Li. Reproduced with permission.[51] Copyright 2016, American Chemical Society.

ADVANCED
SCIENCE NEWS

www.advancedsciencenews.com
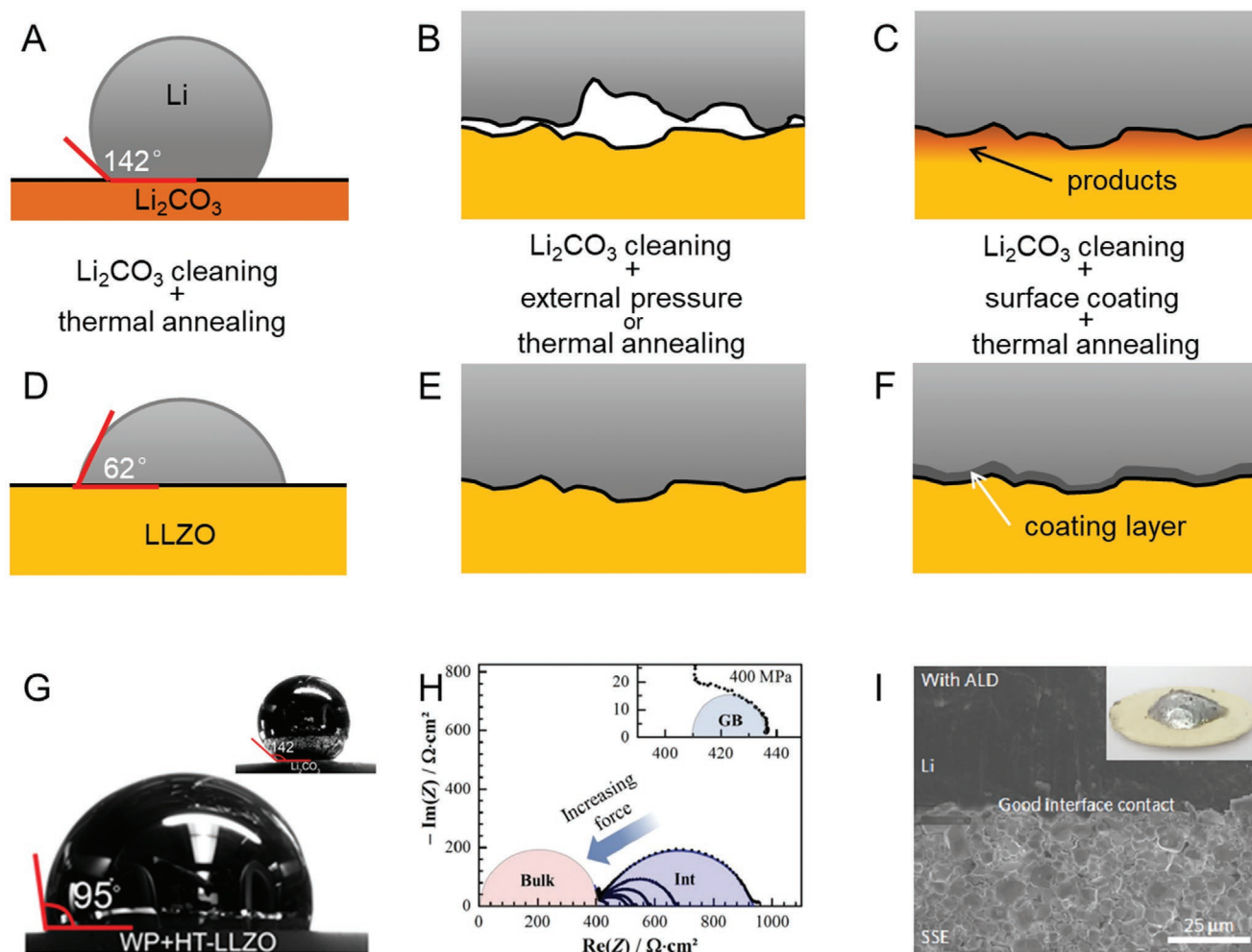
ADVANCED
ENERGY
MATERIALS

www.advenergymat.de

Figure 4. Origin of Li/garnet interfacial resistance and the improving strategies. Origin of interfacial resistance from A) poor wettability of Li to surface impurities Li_2CO_3. Reproduced with permission.[56] Copyright 2017, American Chemical Society. B) Insufficient contact. C) Side reactions. D–F) Strategies for reducing the interfacial resistance. Experiments results of strategies: G) surface cleaning by thermal treatment. Reproduced with permission.[56] Copyright 2017, American Chemical Society. H) External pressure. Reproduced with permission.[57] Copyright 2019, American Chemical Society. I) ALD coating of Al_2O_3. Reproduced with permission. [52] Copyright 2017, Springer Nature.

remained, and only trace of Li_2CO_3, Li_2O_2, and Li_2O were observed (Figure 3B,C). Scanning transmission electron spectroscopy observed an ultrathin tetrahedral $Li_7La_3Zr_2O_{12}$ film between cubic $Li_7La_3Zr_2O_{12}$ and Li, due to the reduction of cubic $Li_7La_3Zr_2O_{12}$ by Li metal (Figure 3D–F).[51] The electronically insulative tetrahedral $Li_7La_3Zr_2O_{12}$ prevented the further reduction of cubic $Li_7La_3Zr_2O_{12}$, keeping the ultrathin film stable at ≈6 nm. $Li_7La_{2.75}Ca_{0.25}Zr_{1.75}Nb_{0.25}O_{12}$ showed a worse stability with Li metal, with surface decomposing into Li_2O/ Li_2O_2, La_2O_3, Zr/Zr_xO, Ca, Nb/Nb_x, and bulk suffering from lattice expansion.[52] The Nb-doped garnets shows a worse stability than Ta-doped garnets, which is in agreement with the research results of Zhu et al.[53] In a brief, the possible reaction products between cubic garnets and Li metal are tetrahedral $Li_7La_3Zr_2O_{12}$, Zr/Zr_xO, Ca, Nb/Nb_x, or Li_2CO_3, Li_2O_2, Li_2O, La_2O_3, which are composition dependent. Most importantly, all the possible products are electronically insulative, preventing the further reduction of the bulk garnets and making the garnet electrolytes suitable for ASSLBs.

2.2. The Origin of Interfacial Resistance

At the beginning, the large interfacial resistance between garnet and lithium metal is assumed to be intrinsic, until surface Li_2CO_3 was found to be the key reason.[27,54,55] DFT calculation predicted that the interfacial work functions of adhesion to lithium are 0.10 J m^{-2}, and 0.67 J m^{-2} for Li_2CO_3 and bare $Li_{6.25}Al_{0.25}La_3Zr_2O_{12}$, respectively, corresponding to contact angles of 142° and 62° (**Figure 4**A,D).[56] The contact angle of Li/ LiOH interface is 125°, similar to Li/Li_2CO_3 interface. This indicates that clean LLZO is lithiophilic intrinsically, and the large interfacial resistance arises from the surface contaminated Li_2CO_3 and LiOH. Experiments showed that larger Li_2CO_3 content on the surface of $Li_{6.25}Al_{0.25}La_3Zr_2O_{12}$ yielded a larger interfacial resistance, demonstrating this prediction.[28] In addition, poor contact between Li metal and garnet electrolytes makes the effective contact area generally smaller than the apparent area, it is another reason for the large interfacial resistance (Figure 4B).[52,57] Moreover, the insulative products of side

ADVANCED
SCIENCE NEWS
www.advancedsciencenews.com

ADVANCED
ENERGY
MATERIALS
www.advenergymat.de

reactions may also contribute to the large interfacial resistance (Figure 4C). The interfacial resistance arising from side reaction is composition dependent, large interfacial resistance was only observed in Nb-doped $Li_7La_3Zr_2O_{12}$ system, while Al-and Ta-doped $Li_7La_3Zr_2O_{12}$ exhibited small interfacial resistances of 100 and 50 Ω cm² respectively.[52,53] This agrees with the stability of garnets with Li. Generally, Li_2CO_3 deriving from the instability of garnets against the air is considered as the major origin of interfacial resistance, poor interfacial contacts, and side reactions between garnets and Li contribute the interfacial resistance as well.

2.3. Strategies for Reducing the Interfacial Resistance

As previous discussion, the large interfacial resistance arises from the poor wettability due to Li_2CO_3 contamination, poor interfacial contacts, and side reactions. Therefore, efforts that increasing the wettability of Li, enhancing the interfacial contacts and avoiding side reactions, are expected to reduce the interfacial resistance. These strategies include surface cleaning, lithium annealing,[58,59] external pressure,[60] and artificial interlayer. Therein, lithium annealing is always cooperated with other techniques in order to improve the effective contacts by softening/melting Li metal, thereby decreasing the interfacial resistance.[58,59]

2.3.1. Surface Cleaning

As Li_2CO_3 and LiOH is the major origin of the large interfacial resistance, surface cleaning can increase the contact angle of Li metal and LLZO up to 62° theoretically (Figure 4D). The strategies of surface cleaning include: 1) Physical polishing. Physical polishing is the most convenient way to remove surface Li_2CO_3 and LiOH. Physical polishing of Al-doped $Li_7La_3Zr_2O_{12}$ under Ar atmosphere without Li annealing, resulted an interfacial resistance of 109 Ω cm².[27] 2) Chemical treatment. Researches applied dilute/weak acid to remove Li_2CO_3 by chemical reaction, typical examples are HCl and H_3PO_3. After chemical treatment by HCl and H_3PO_3, the interfacial resistances were reduced to 26 and 7.0 Ω cm², respectively.[61,62] However, the Li^+/H^+ exchange needs special attention and further study during this process. 3) Thermal decomposition. Thermal decomposition of Li_2CO_3/LiOH is another way to achieve clear LLZO. LiOH is likely to decompose at a relatively low temperature. With the increase of annealing temperature, the LiOH content decreased, as well as the interfacial resistance. After annealing at 500 °C, the contact angle to Li reduced to 95° and the interfacial resistance reached 2 Ω cm² (Figure 4G).[56] Li_2CO_3 decomposition needs a higher temperature. After calcination at 900 °C for 24 h, Li_2CO_3 decomposed, and a low interfacial resistance of 49 Ω cm² was achieved.[63] Introduction of reductive carbon decreased the decomposition temperature of Li_2CO_3 down to 700 °C, resulting an interfacial resistance of 28 Ω cm².[64] Interestingly, Cheng et al. claimed that Li_2CO_3 can be removed at 250 °C in an inert atmosphere, taking the advantage of inverse reaction of Li^+/H^+ exchange. This low calcination temperature was not reported in other researches, and an interfacial resistance

of 178 Ω cm² was achieved.[31] The different interfacial resistance in researches might be due to the residual Li_2CO_3/LiOH content on the garnet surface, coming from the ability of each strategies in removing Li_2CO_3/LiOH. The detailed treatment and performance are listed in **Table 1**.

2.3.2. External Pressure

Unlike Li annealing, which increases the lithium fluidity at high temperature, external force accelerates Li creeping at room temperature, thereby facilitating Li to fill the gaps and increasing the effective contacts (Figure 4E). Theory of electrical constriction resistance was applied to understand the relationship between the effective contact area and applied external load.[65] The interfacial resistance follows Equation (1), its value is dependent on the applied force, mechanical and electrical properties of the contacted materials.[60] Because the ionic conductivity of $Li_{6.25}Al_{0.25}La_3Zr_2O_{12}$ is much lower than the electronic conductivity of Li metal, and the Vickers hardness of Li ($H_{Li} \leq 5$ MPa) is much lower than that of garnet, the interfacial resistance is determined by the electrical properties of $Li_{6.25}Al_{0.25}La_3Zr_2O_{12}$ and the plastic properties of Li. For a specific SE, the contact area and interfacial resistance is solely dominated by the Li deformation with external force. Figure 4H shows that with the increase of external force, the interfacial resistance between $Li_{6.25}Al_{0.25}La_3Zr_2O_{12}$ and Li metal decreases continuously, and reaches nearly zero under 400 MPa[57]

$$R_{int} = \frac{\rho}{2}\sqrt{\frac{\pi H}{F}} = \frac{1}{2\sigma_{Li+}}\sqrt{\frac{\pi H_{Li}}{F}} \tag{1}$$

Therein, ρ denotes the resistivity, σ_{Li+} denotes the ionic conductivity of $Li_{6.25}Al_{0.25}La_3Zr_2O_{12}$, F denotes the applied external force, and H denotes the Vickers Hardness. It should note that the equation is not applicable at a very high force.

2.3.3. Artificial Interlayer

Introduction of an artificial interlayer onto LLZO surface is a typical way, not only to increase the wettability of lithium metal, but also to avoid the possible side reactions between Li and garnets (Figure 4F). Two categories are summarized by their affecting mode. One group is materials that can form lithium alloys or Li-intercalated compounds. The typical examples are Au,[66] Ag,[67] Al,[68] Cu,[69] Ge,[70] Si,[71] and graphite[72–74] which can form Li/Au, Li/Ag, Li/Al, Li/Ge, Li/Si alloys, and lithiated graphite during the thermal annealing process. The alloying or lithiated process increased the wettability of Li and reduced the interfacial resistance to tens of ohms (Table 1). The other group is materials that can react with Li metal, therefore increasing the wettability of Li. The materials include Al_2O_3,[46] ZnO,[42] SnO_2,[75] SnF_2,[76] MoS_2,[77] $AgNO_3$,[78] Cu_3N,[79] and Cu_6Sn_5.[80] They play a similar role in increasing the wettability, so here we take Al_2O_3 as an example. Han et al. introduced an ultrathin Al_2O_3 onto the surface of $Li_7la_{2.75}Ca_{0.25}Zr_{1.75}Nb_{0.25}O_{12}$ by atomic layer deposition, then the Al_2O_3 was transformed

**ADVANCED
SCIENCE NEWS**
www.advancedsciencenews.com

**ADVANCED
ENERGY
MATERIALS**
www.advenergymat.de

Table 1. Strategies of initial Li/garnet interfacial building and corresponding electrochemical performance.

Composition	Strategies		ASR [Ω cm^2]	j [mA cm^{-2}]	Li electrodeposit	Reference
	Garnet surface	Li/LLZO interface			[mAh cm^{-2}]	
Al-doped Li$_7$La$_3$Zr$_2$O$_{12}$	Surface polish	Simple attach	109	0.046	0.092	[27]
Li$_{6.25}$Ga$_{0.25}$La$_3$Zr$_2$O$_{12}$	900 °C, surface polish	350 °C, 10 min	49	0.3	0.075	[63]
Li$_{6.4}$La$_3$Zr$_{1.4}$Ta$_{0.6}$O$_{12}$	HCl treatment	200 °C, 30 min	26	0.2	0.1	[61]
Li$_{6.5}$La$_3$Zr$_{1.5}$Ta$_{0.5}$O$_{12}$	H$_3$PO$_3$ treatment	200 °C	7.0	0.5	0.25	[62]
Li$_{6.25}$Al$_{0.25}$La$_3$Zr$_2$O$_{12}$	Wet polish, 500 °C annealing	175 °C, 12 h	2	0.2	0.1	[56]
Li$_{6.5}$La$_3$Zr$_{1.5}$Ta$_{0.5}$O$_{12}$	Carbon, 700 °C annealing	Simple attach	28	0.1	0.03	[64]
Al-doped Li$_7$La$_3$Zr$_2$O$_{12}$	250 °C, 12 h annealing.	0.2 MPa press	178	–	–	[31]
Li$_{6.75}$La$_3$Zr$_{1.75}$Ta$_{0.25}$O$_{12}$	Surface polish	150 MPa press	20	–	–	[60]
Li$_{6.25}$Al$_{0.25}$La$_3$Zr$_2$O$_{12}$	Surface polish	400 MPa press	<1	0.1	1.2	[57]
Li$_{6.6}$La$_3$Zr$_{1.6}$Ta$_{0.4}$O$_{12}$	Au coating	100 °C, 0.1 MPa, 5 h	190	0.08	≈0.04	[66]
Li$_7$La$_{2.75}$Ca$_{0.25}$Zr$_{1.75}$Nb$_{0.25}$O$_{12}$	Ag coating	200 °C, 3980 Pa, 10 min	66	0.2	0.1	[67]
Li$_7$La$_{2.75}$Ca$_{0.25}$Zr$_{1.75}$Nb$_{0.25}$O$_{12}$	Al coating	200 °C	≈75	0.2	0.017	[68]
Li$_{6.85}$La$_{2.9}$Ca$_{0.1}$Zr$_{1.75}$Nb$_{0.25}$O$_{12}$	Ge coating	200 °C, 10 min	115	0.1	0.008	[70]
Li$_{6.85}$La$_{2.9}$Ca$_{0.1}$Zr$_{1.75}$Nb$_{0.25}$O$_{12}$	Si coating	200 °C, 20 min	127	0.2	0.003	[71]
Li$_7$La$_{2.75}$Ca$_{0.25}$Zr$_{1.75}$Nb$_{0.25}$O$_{12}$	ZnO coating	300 °C, 30 min	20	0.1	0.017	[48]
Li$_7$La$_{2.75}$Ca$_{0.25}$Zr$_{1.75}$Nb$_{0.25}$O$_{12}$	Al$_2$O$_3$ coating	250 °C, 0.26 psi, 1 h	1	0.2	0.1	[52]
Li$_{5.9}$Al$_{0.2}$La$_3$Zr$_{1.75}$W$_{0.25}$O$_{12}$	Graphite coating	210 °C, 0.5 h	<20	0.3	0.3	[73]
Li$_{5.9}$Al$_{0.2}$La$_3$Zr$_{1.75}$W$_{0.25}$O$_{12}$	Graphite coating	210 °C, 0.5 h	<20	0.5	3	[73]
Li$_{6.5}$La$_3$Zr$_{1.5}$Ta$_{0.5}$O$_{12}$	Li-C paste	250 °C	11	0.8	0.4	[72]
Li$_{6.4}$La$_3$Zr$_{1.4}$Ta$_{0.6}$O$_{12}$	SnO$_2$ coating	200 °C, 1 h	25	0.2	0.1	[75]
Li$_{6.75}$La$_3$Zr$_{1.75}$Ta$_{0.25}$O$_{12}$	SnF$_2$ coating	280 °C, 2 min	21	0.05	0.025	[76]
Li$_{6.5}$La$_3$Zr$_{1.5}$Ta$_{0.5}$O$_{12}$	MoS$_2$ coating	100 °C, 2 h	14	0.2	0.1	[77]
Li$_{6.5}$La$_3$Zr$_{1.5}$Ta$_{0.5}$O$_{12}$	AgNO$_3$	220 °C, 2 min	4.5	0.5	0.25	[78]
Li$_7$La$_{2.75}$Ca$_{0.25}$Zr$_{1.75}$Nb$_{0.25}$O$_{12}$	Cu$_6$Sn$_5$		236	0.25	0.125	[80]

to Li$_x$Al$_2$O$_{3+x/2}$ (x = 0.4 to 1.4) upon thermal treatment with Li metal. Li$_x$Al$_2$O$_{3+x/2}$ with a higher binding energy of 6.0–11.4 eV nm^{-2} than that of 1.6 eV nm^{-2} for Li$_2$CO$_3$, increased the contact angle and decreased the interfacial resistance to 1 Ω cm^2 (Figure 4I).[52] The detailed treatment and performance are listed in Table 1.

In a short summary, the large interfacial resistance arises from the contamination of LiOH and Li$_2$CO$_3$ from the air, insufficient interfacial contacts and side reactions between Li metal and garnet electrolytes. The strategies, surface cleaning improved the wettability of garnet to Li, Li annealing and external pressure enhanced the effective interfacial contacts, artificial interlayer not only facilitated the wettability of Li to garnet but also avoided side reactions, these all reduced the interfacial resistance. In general, multimodal strategies are employed collaboratively for the best interfacial properties.

2.4. Lithium Stripping and Plating

Even though a good Li/garnet interface is initially built, its dynamic change during stripping and plating process is still inevitable, and is detrimental to the long-term cycling.[57,81]

Therefore, the interfacial stability of Li/garnet during stripping and plating process needs special attention. Typically, in a symmetric Li/SE/Li cell, the overall interfacial resistance increased during stripping process and decreased during the subsequent plating process, the overall interfacial resistance increased with the following cycling (**Figure 5**A,B).[81] Wang et al. employed Ni as reference electrode and decoupled the contribution of Li stripping electrode and Li plating electrode.[82] The results showed that the resistance evolution happened at the Li stripping electrode, while the resistance of Li plating electrode kept constant. In addition, Janek and co-workers pointed out the stripping process can be denoted by Kroeger–Vink–Notation equation[57]

$$Li \leftrightarrow \left[Li_{Li+}^X (LLZO) - V'_{Li+} (LLZO)\right] + e'(Li) + V_{Li}^X (Li) \tag{2}$$
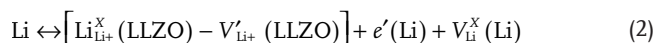
During stripping process, when a Li$^+$ passes through the Li/garnet interface from Li metal to garnets, an electron e'(Li), and a vacant site V_{Li}^X(Li) are left in the lithium metal surface, and the Li$^+$ occupies an available vacant site V'_{Li+} +(LLZO) or an interstitial site in the garnet. These vacancies formed in Li metal can either annihilate after repeatable growth or diffuse from the interface into the bulk. Because the charge transfer
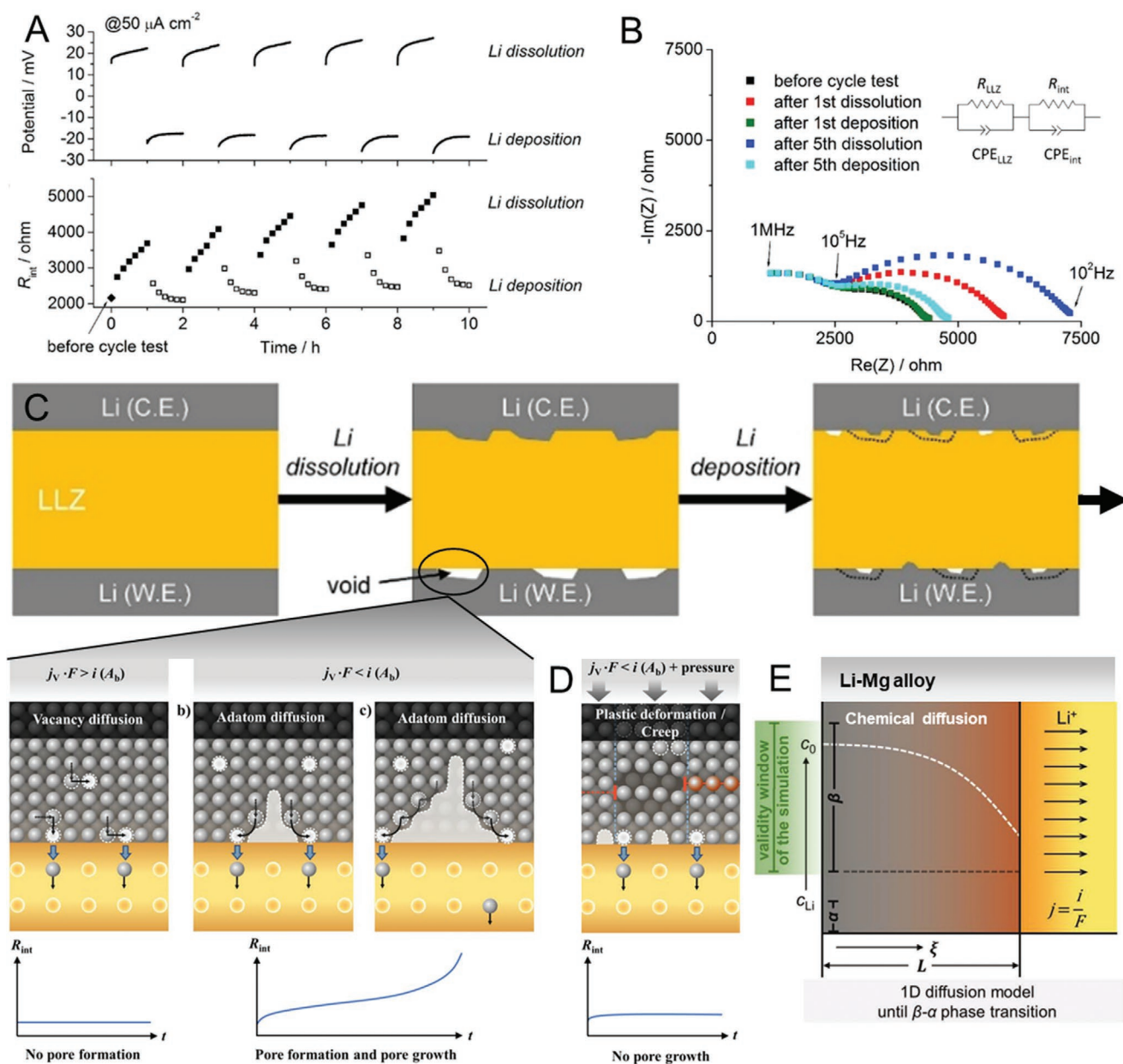
Figure 5. Schematic illustration of the dynamic changes at the Li/garnets interface during repeated Li stripping/plating process. A) Evolution of potential and interfacial resistance during lithium dissolution and deposition. Reproduced with permission.[81] Copyright 2017, American Chemical Society. B) Impedance evolution after repeated cycles. Reproduced with permission.[81] Copyright 2017, American Chemical Society. C) Schematic illustration of the lithium transport and morphological evolution of the interface for a lithium metal electrode. Reproduced with permission.[57] Copyright 2019, American Chemical Society. Reproduced with permission.[81] Copyright 2017, American Chemical Society. D) The role of external pressure in maintaining the surface morphology. Reproduced with permission.[57] Copyright 2019, American Chemical Society. E) Schematic illustration of the lithium transport and morphological evolution of the interface for a Li–Mg alloy electrode. Reproduced with permission.[85] Copyright 2019, Wiley-VCH.

resistance is quite small and the Li$^+$ mobility in bulk garnets is very high, vacancy diffusion in Li metal dominates the interfacial dynamics when vacancy annihilation is excluded for simplicity. 1) If the diffusion coefficient of vacancies in Li metal is high enough, a dynamic balanced vacancy concentration at the interface will be established and the interface will keep morphologically stable. 2) If the applied current density exceeds this vacancy diffusion limit, the vacancies will supersaturate

and accumulate to pores at the interface. Adatom diffusion along pore surfaces is typically faster than vacancy diffusion in bulk, pores will grow three-dimensionally.[57] The contact loss then results in an increase of interfacial resistance (Figure 5C). On the other hand, when the polarization is switched, the pores formed during Li stripping process will be partially filled up during the subsequent Li plating process. Therefore, the interfacial resistance decreases. After 1st cycle, the contact area of

interface becomes smaller than that at the beginning, and the overall interfacial resistance increases. The pores gradually accumulate at the interface during cycling, resulting in a continuous increase of interfacial resistance.

Clearly, the increase of interfacial resistance arises from the formation of voids at anode interface, when the flux of Li toward the interface from diffusion in the lithium metal is insufficient to replenish the flux of Li being dissolved and migrated through the LLZO electrolyte. Therefore, two directions are helpful to prevent the formation of voids at the interface instead of sacrificing the current density. The first strategy is increasing the lithium creep. External pressure is in favor of lithium creep due to the plastic deformation of lithium metal, therefore preventing pore formation and stabilizing the interface during stripping process (Figure 5D).[57] Moreover, a higher external pressure, a higher creep rate of Li metal, and better interfacial stability.[82] However, high pressures in GPa range are expected to achieve stable current densities ranging to 10 mA cm^{-2}, which will increase the weight and cost of batteries. The second strategy is increasing the Li diffusion in anode. Compared to pure Li metal anode, Li-rich alloys exhibiting a higher Li$^+$ diffusion coefficient, were applied to maintain the interfacial stability.[83–85] Moreover, Li-rich alloys exhibited a different kinetic limitation during stripping process compared to pure Li metal. Instead of the formation of the voids at interface, the chemical diffusion of Li$^+$ in alloy becomes the limitation process (Figure 5E). Therefore, external pressure will not maintain the interfacial kinetics. Instead, high temperature can greatly improve the diffusion kinetics of alloys, therefore maintaining the interfacial resistance.

2.5. Lithium Dendrite

SEs are expected to prevent lithium dendrite and to revive Li metal anode. According to Monroe model, SEs with a twice shear modulus of lithium metal can prevent the lithium dendrites.[7] The garnet electrolytes with a shear modulus of ≈60 GPa, are far than enough to prevent the lithium dendrite theoretically.[8] However, lithium dendrites are still observed in garnet-based cells when the current density reaches a critical value, causing the short circuit of batteries. The current density at and above which Li metal can propagate through the SE is defined as critical current density (CCD).[86] The short-circuit period decreased with the increased current density beyond the CCD.[87] Moreover, Han et al. proposed that a necessary low potential in SE smaller than the lithium plating potential is required for lithium dendrite, as a supplementary prerequisite to CCD.[88] Morphologically, lithium dendrites were always observed at specific spots on garnet surface (**Figure 6**A), and preferentially existed along the cracks, open pores, and grain boundaries in bulk garnet (Figure 6B–D).[89–92] In addition,
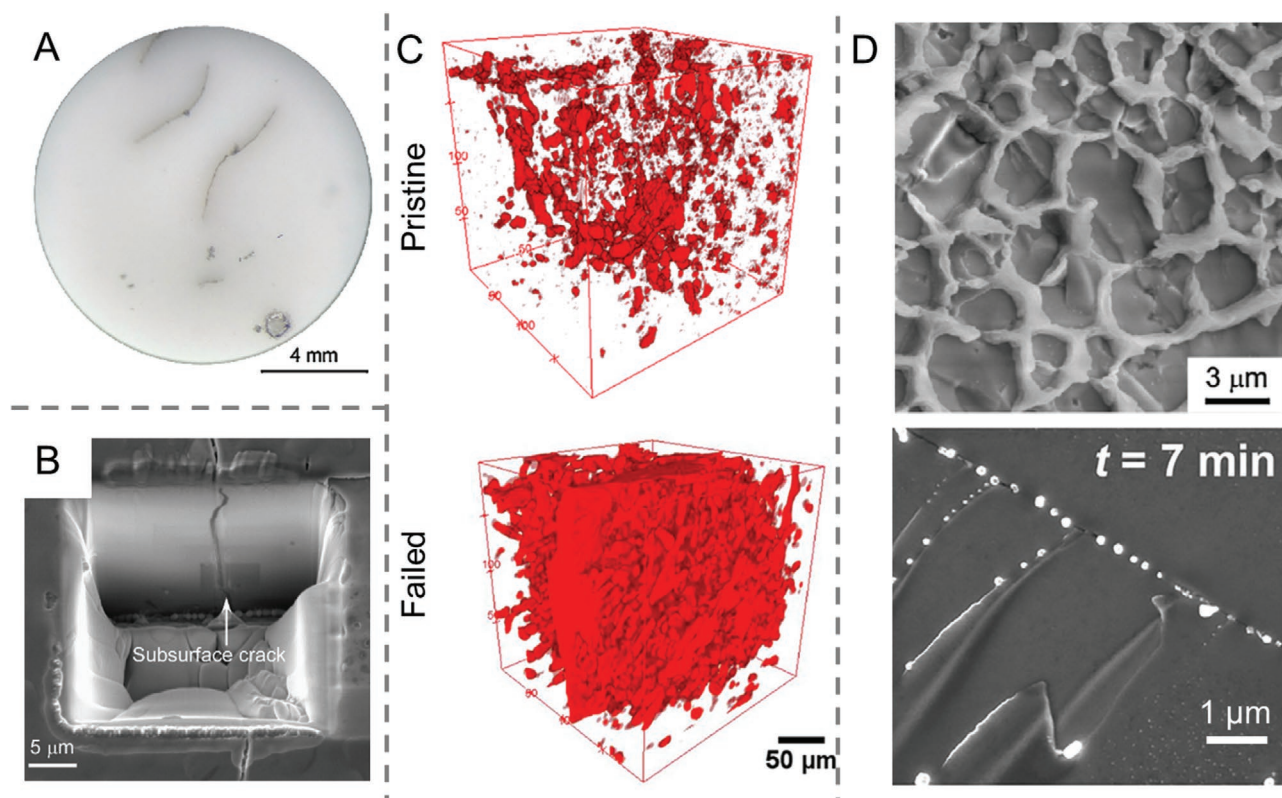
Figure 6. Lithium dendrite in solid electrolyte. A) Optical image of lithium dendrite in garnet electrolyte. Reproduced with permission.[91] Copyright 2017, Elsevier B.V. The formation of lithium dendrite in B) cracks. Reproduced with permission.[91] Copyright 2017, Elsevier B.V. C) Pores. Reproduced with permission.[92] Copyright 2018, American Chemical Society. D) Grain boundaries. Reproduced with permission.[89] Copyright 2019, Elsevier Inc. Reproduced with permission.[91] Copyright 2017, Elsevier B.V.

**ADVANCED
SCIENCE NEWS**

www.advancedsciencenews.com

**ADVANCED
ENERGY
MATERIALS**

www.advenergymat.de

lithium dendrites also happened in a single crystal with pre-existed cracks, indicating the lithium dendrite not only grow through the pores, cracks, grain boundaries, but also can penetrate the grains.[93]

2.5.1. Growth Mechanism of Lithium Dendrite

The nucleation and growth mechanism of lithium dendrite should be highly correlated to plating process, but is still unclear. Two typical mechanisms are summarized, that is continuous root-growth mechanism and sporadic bulk-growth mechanism.

Continuous Root-Growth Mechanism: Continuous root-growth mechanism suggests Li nucleates at the Li/SE interface and penetrates through the SE. When lithium dendrite reaches the

cathode side, the short circuit will happen. Lithium dendrite begins with nucleation at Li/SE interface. However, state-of-the-art, two opinions dominate the lithium nucleation process. 1) Based on local electrochemomechanical model, Raj and Wolfenstine predicted the nucleation occurs when (**Figure 7**A)[86]

$$jf\rho d\left(1-\alpha\right)|e| \geq \frac{2\gamma\Omega_{Li}}{r_c} + \sigma_F\Omega_{Li}; f = \left(1-\frac{\rho_d}{\rho}\right)f; \alpha = \frac{d'}{d} \quad (3)$$

wherein j is current density, ρ is overall resistivity, ρ_d is matrix resistivity, d is crystallite size, d' is the distance between grain boundary and lithium metal electrode, Ω_{Li} is lithium density per volume, γ is normal strain, r_c is the diameter of dendrites, σ_F is fracture stress of ceramics. The left hand is the electro-chemo driving force of nucleation, while the right hand is the
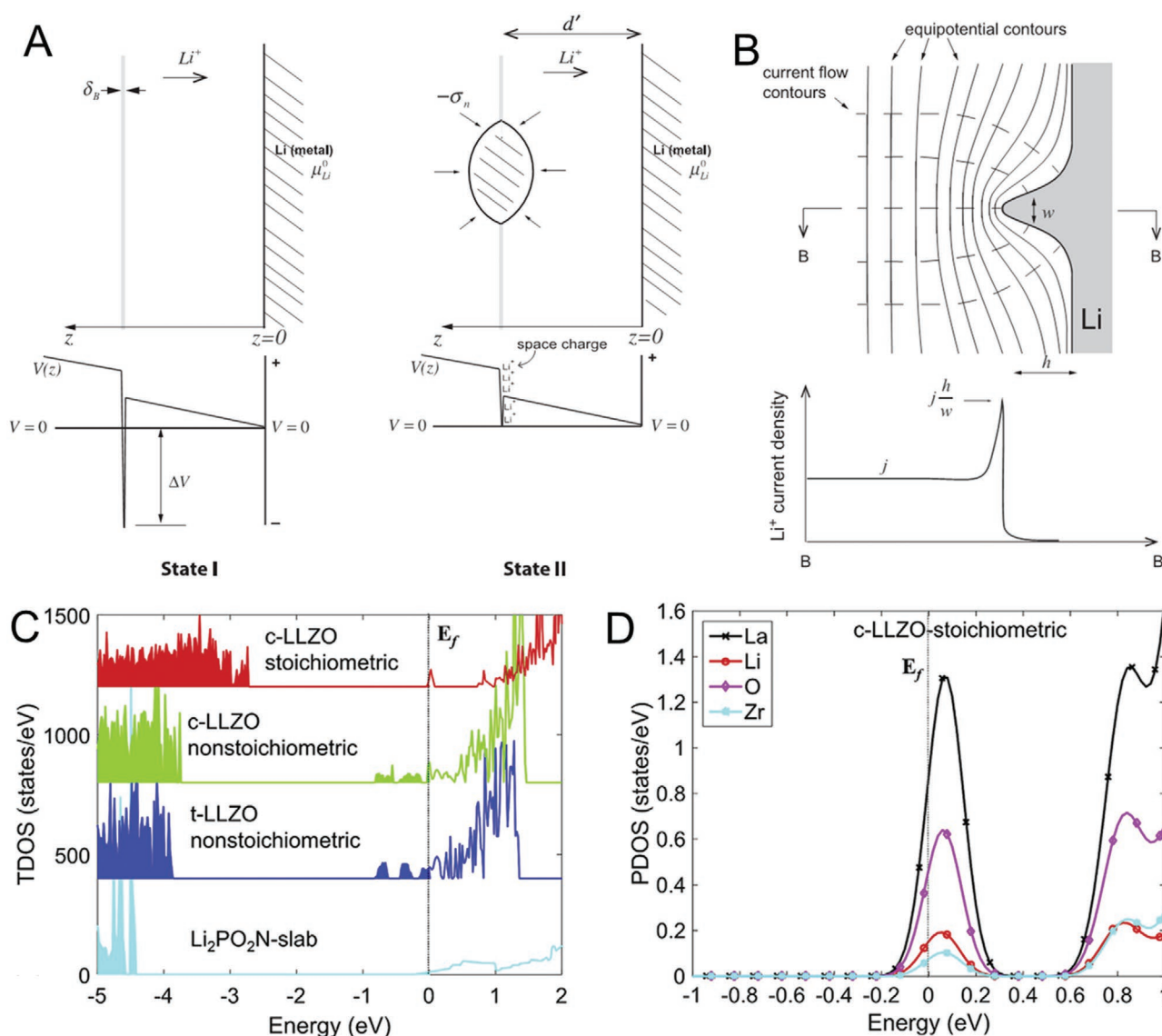
Figure 7. Theoretical predication of nucleation and growth mechanism of lithium dendrite in solid electrolyte. Electrochemomechanical model for A) nucleation and B) growth of lithium dendrite in solid electrolyte. Reproduced with permission.[86] Copyright 2017, Elsevier B.V. C) Total density of states (TDOS) of $Li_7La_3Zr_2O_{12}$. D) Partial density of states (PDOS) of stoichiometric cubic $Li_7La_3Zr_2O_{12}$. Reproduced with permission.[99] Copyright 2018, Elsevier B.V.

ADVANCED
SCIENCE NEWS
www.advancedsciencenews.com

ADVANCED
ENERGY
MATERIALS
www.advenergymat.de

mechanical opposing force. The opposing force includes the surface energy to add a lithium embryo at the interface under compressive traction, and strain energy induced in the surrounding matrix. Therefore, high conductivity (low ρ), large strain, and high fracture stress of ceramics are expected to prevent dendrite nucleation. 2) Wang et al. reported that sluggish Li^0 transport is the reason for the lithium nucleation.[94] The lithium nucleation depends on the Li flux toward/away from the Li/SE interface. Therein, Li flux toward the interface is determined by the current density, Li flux away from the interface is dominated by the Li diffusion and creep (assuming a nonzero stack pressure). On the one hand, at low current densities, Li^+ flux toward the interface is relatively small, Li° flux away from the interface is sufficiently fast to maintain a planar geometry. On the other hand, at high current densities, Li^+ flux toward the interface is much larger than Li° flux away from the interface. Therefore, Li atoms plate on "nonplanar" sites and eventually produce Li^0 pile-up.

Briefly, two opinions both agree that a critical current is required. Raj et al. proposed this current density is used to overcome the mechanical opposing force of SE, and Wang et al. believed this current density should overwhelm the Li flux away from the interface. Furthermore, these nuclei or pile-ups are strongly affected by the surface geometry, they are preferentially happened at the defect flaws, where the electric field is stronger.[95] In addition, the poor contact and impurity Li_2CO_3 between Li metal and SE accelerate this localized plating.

After lithium dendrite nucleates at the interface, it will propagate into the bulk SE upon further polarization. Theoretically, local current density will concentrate at the tip of protuberance (nuclei), denoted as j_{int}, which will promote dendrite growth (Figure 7B).[86] According to St. Venant' principle

$$j_{int} = j \frac{h}{w} \tag{4}$$

wherein j is the average current density going through the electrolyte, h is the distance of the tip from lithium surface, and w is the width of nuclei. Considering the back stress σ_F, which will hinder the dendrite growth, the overall potential should be

$$\Delta \mu_{Li}^{int*} = |e| k_{int} j \frac{h}{w} - \sigma_F \Omega_{Li} \tag{5}$$

wherein k_{int} is the interfacial area specific resistance. For the incipient growth of lithium dendrite, it requires $\Delta \mu_{Li}^{int*} > 0$. After the incipient growth, the opposing force should be determined by the fracture toughness, instead of fracture strength of the ceramic electrolytes.

According to Monroe model, SEs with a twice shear modulus of lithium metal can prevent the lithium dendrites. Two explanations are summarized for the observed lithium dendrite. On the one hand, practical Li modulus is found to be higher than the theoretical one. The Young's modulus of Li whiskers measured by Zhang et al. are between 2.7 and 21 GPa, and the yield strength ranges from 12.2 to 244 MPa, much higher than that of bulk polycrystalline Li.[96] On the other hand, grain boundaries, pores, and cracks exhibit a lower shear modulus than the perfect crystals. Molecular dynamics simulations performed on tile and twist boundaries revealed that the shear modulus of grain boundary is up to 50% smaller than that in bulk regions. These

effects could arise from deviations in density and atomic structure near the grain boundaries.[97]

In a short summary, continuous root-growth mechanism suggests that lithium nucleation preferentially happens at the flaws at the Li/SE interface. The stress accumulation in lithium metal and surrounding SE causes cracks in SE. The lithium metal propagates along the cracks and fills up the empty spaces. The stress accumulates in the newly formed lithium metal again and causes the crack again. The process repeats until the lithium dendrite reaches the counter electrode, causing a short circuit. In addition, although Li nucleation preferentially happens at pores and flaws, Li may also accumulate near electrode/grain boundaries junctions via interfacial diffusion/creeping away from the stiffer bulk regions. The lithium dendrite penetrates along the soft grain boundaries, cracks, and pores, where are energy preferable (**Figure 8**A).[97,98]

Sporadic Bulk-Plating Mechanism: Sporadic bulk-plating mechanism suggested that Li plating (nucleation) might happen in SE instead of at the Li/SE interface, and continuous Li plating are not necessary for the short circuit (Figure 8B). Two critical conditions have to be satisfied simultaneously: the presence of mobile electrons in SE, and a lower potential in SE than the Li plating potential. A higher electronic conductivity of SE results in a lower potential in SE, which will supply a larger driving force for dendrite formation.[88] Furthermore, the potential at local positions can fluctuate widely, dependent on the microstructure and composition heterogeneities in SE, especially at defects such as impurities, grain boundaries and pores. Based on density functional theory, Tian et al. calculated the total density of states of $Li_7La_3Zr_2O_{12}$ at interfaces and grain boundaries are different from that of the bulk. The nonstoichiometric surfaces of c-$Li_7La_3Zr_2O_{12}$ and t-$Li_7La_3Zr_2O_{12}$ are electronic conductive since the Fermi levels have already moved into the conduction band (Figure 7C). Therefore, the surface state could trap external electrons because it does not connect with conduction bands. The partial density of state shows that the excess electrons locate around the La atoms. The Li^+ is reduced by the electrons from the La and nucleates at the interfaces and grain boundaries (Figure 7D).[99] In addition, besides a higher electronic conductivity, the fracture stress should be lower at defects, thereby increasing the driving force and decreasing the opposing force. Therein, electronic conductivity is believed to play a more important role in lithium dendrite compared to mechanical properties of SE.[100]

Despite the theoretical deduction, the experiment results on the nucleation and growth mechanism of lithium dendrite is still controversial. Kilner and co-workers applied operando optical spectroscopy to characterize the Li propagation in Ga-doped $Li_7La_3Zr_2O_{12}$.[101] They directly observed the formation of transgranular cracks by lithium penetration, then the transgranular cracks were filled by new lithium dendrite, which caused the further cracks. The process repeated until short circuit (**Figure 9**A). Grey et al. observed a continuous lithium growth in garnet-type $Li_{6.5}La_3Zr_{1.5}Ta_{0.5}O_{12}$ via ^7Li NMR chemical shift imaging (Figure 9B).[89] These experiments support the continuous root-growth mechanism. Han et al. applied neutron depth profiling to investigate the lithium distribution in SEs. They found that the lithium distributed uniformly in the bulk of $Li_{6.4}La_3Zr_{1.4}Ta_{0.6}O_{12}$, Li_3PS_4, and LiPON from

**ADVANCED
SCIENCE NEWS**
www.advancedsciencenews.com
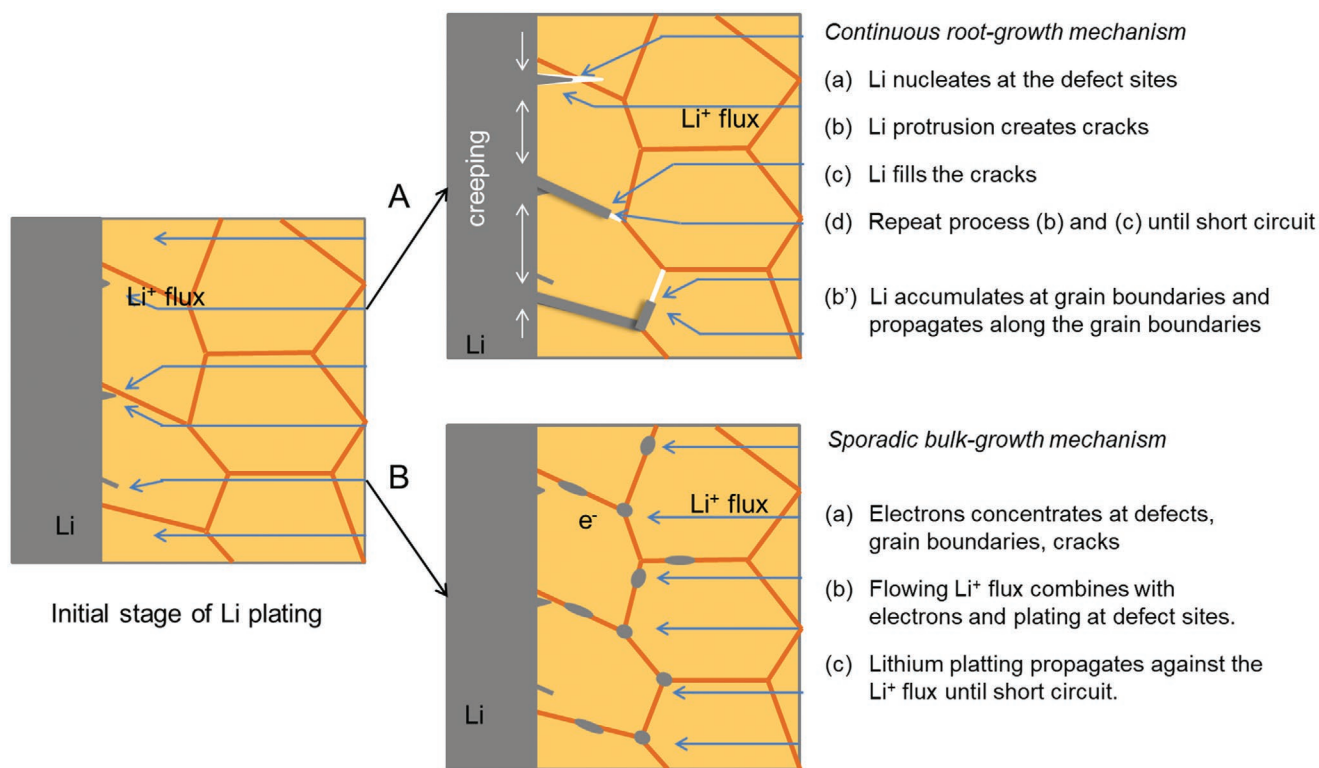
**ADVANCED
ENERGY
MATERIALS**
www.advenergymat.de

Figure 8. Schematic illustration of lithium dendrite mechanism in polycrystalline electrolyte. A) Continuous root-growth mechanism. B) Sporadic bulk-growth mechanism.

the lithium metal to cathode side (Figure 9C). Furthermore, CCD of $Li_{6.4}La_3Zr_{1.4}Ta_{0.6}O_{12}$ and Li_3PS_4 were 50 µm cm^{-2} and 120 µA cm^{-2}, while no short circuit happened below 300 µA cm^{-2} in LiPON, showing an opposite trend to their electronic conductivity.[88] Song et al. increased the CCD by introduction of an electronic insulative glass fiber wetted by organic electrolyte, due to the cut off of the electronic conduction.[102] These results support the sporadic bulk-plating mechanism.

Briefly, continuous root-growth mechanism suggests Li nucleates at the anode interface, and penetrates through the SE to cathode side continuously. The driving force is highly correlative to the external current density and the Li/LLZO interfacial properties. By contrast, sporadic bulk-plating mechanism suggests Li nucleation happens in SE, and continuous dendrite is not necessary for the short circuit. The driving force is dependent on the external potential and intrinsic electronic properties of SE. Although the nucleation process is controversial, two mechanisms both agree that the opposing force is related to the mechanical properties of SE. The open pores, cracks, and grain boundaries with lower fracture stress and smaller opposing force, are preferential for lithium dendrite.

2.5.2. The Factors Affecting the CCD

The CCD, representing the ability of SE preventing the lithium dendrite, is an important parameter for practical application, and typically 10 mA cm^{-2} is required. Many factors that affecting either the driving force, or the opposing force of

nucleation and growth, will affect the CCD of lithium dendrite. However, the reasons are not quite clear because of the controversial nucleation and growth mechanism of lithium dendrite.

Interfacial Microstructure: The interfacial microstructure affects the CCD via controlling the current distribution and Li plating. Typically, the insufficient contact and poor wettability between Li metal and SE would cause uneven current distribution and Li plating, thereby accelerating the lithium dendrite and decreasing the CCD. Usually, intimate interfacial contact could yield a small interfacial resistance. Therefore, interfacial resistance could be a valuable parameter to estimate the effective contact. Most results support low interfacial resistance is in favor of Li dendrite free, and typical strategies reducing the interfacial resistance as discussed above can increase the CCD.

Therein, two groups of the strategies can be summarized by their contribution. 1) The intimate and clear interface. In this case, a larger effective contact area results in small interfacial resistance and even current distribution, thereby increasing the CCD. Typical examples, such as physical polishing to remove the contaminated Li_2CO_3,[28] thermal-treatment,[81,103] external pressure,[95] composition tuning,[104] are demonstrated to increase the CCD. 2) The intimate interface with an artificial interlayer. The first role of artificial interlayer is improving the lithium wettability and increase interfacial contact. A typical example is Au deposition, which improved the contact between $Li_{6.6}La_3Zr_{1.6}Ta_{0.4}O_{12}$ and Li metal (**Figure 10**A) and dramatically reduced the interfacial resistance, resulting in short-circuit free when operation at a current density of 0.5 mA cm^{-2}.[66] The second role of artificial interlayer is to be a current collector,
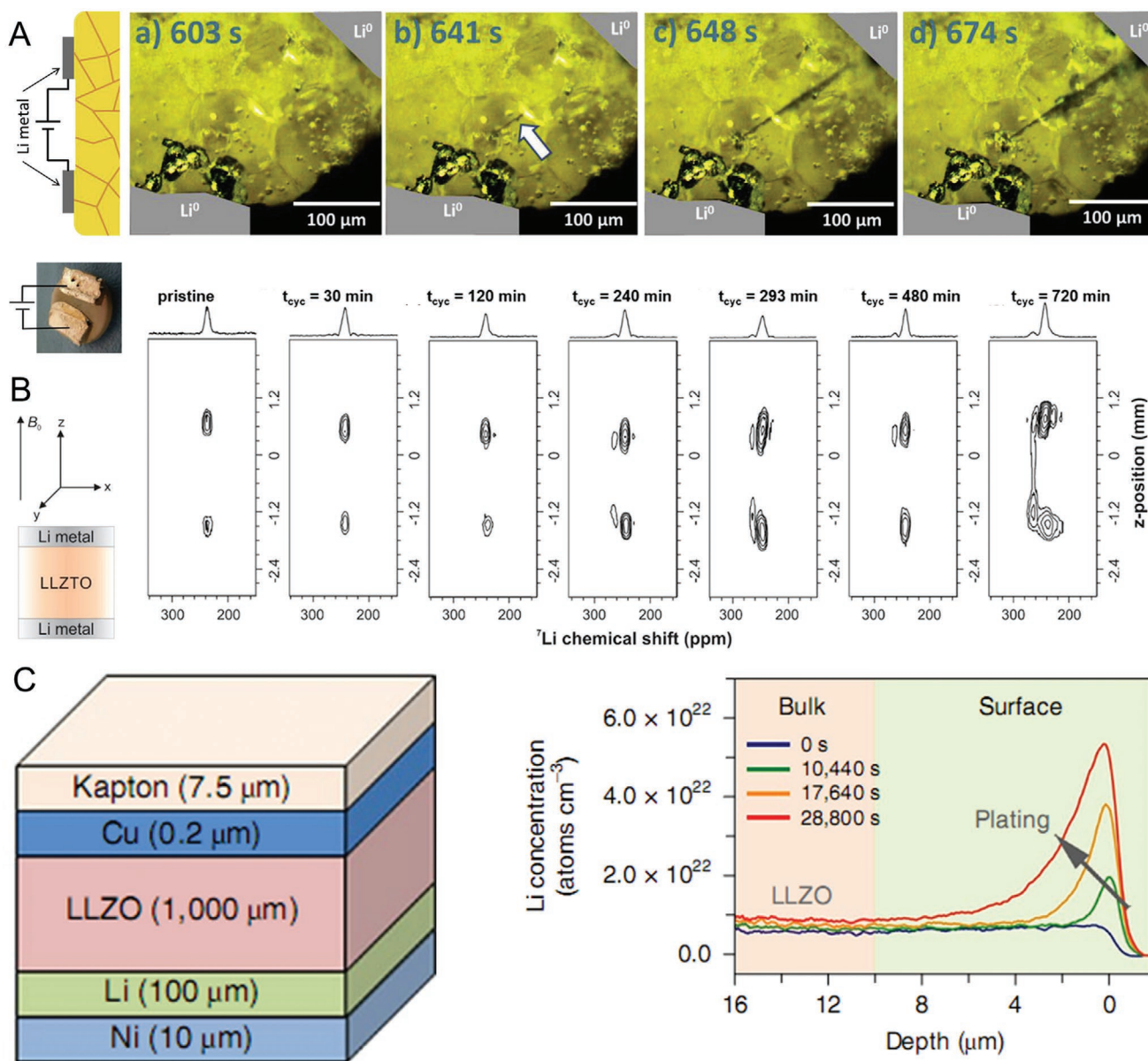
Figure 9. Experimental demonstration of lithium dendrite in garnet. A) In situ optical observation of lithium dendrite growth. Reproduced with permission.[101] Copyright 2018, Elsevier B.V. B) In situ observation of lithium dendrite by nuclear magnetic image. Reproduced with permission.[90] Copyright 2019, American Chemical Society. C) Illustration of set-up and Li concentration profile from neutron depth profile. Reproduced with permission.[88] Copyright 2019, Springer Nature.

which affects the Li nucleation and regulates the interfacial kinetics. Kim et al. and Krauskopf et al. separately studied the role of current collector by surface coating or attaching. They both found the interfacial kinetics should be modified by composition of current collector/coating layer.[95,105] Unlike formation of lithium protrusion at the defects using Li metal as current collector, it formed a lithium alloy when using metal as a current collector. Thereafter, Li rapidly diffused laterally from the defects to other regions because of chemical potential gradient of Li within alloys, converting the whole current collector into a lithium rich alloy. The lithium began to nucleate from the lithium rich alloy phase when the lithium concentration becomes critical or oversaturated. In this way, the lithium plating behavior is changed by the distinct nucleation, and its kinetics is dependent on alloying properties of metal materials, following Ag > Au > Cu.[95] The third role of the artificial layer is filling out the defects and preventing the lithium dendrite. Wu et al. filled the nano Si into the pores and cracks on the surface of $Li_{6.1}Ga_{0.3}La_3Zr_2O_{12}$, the filled Si reacted with the lithium dendrite reversibly during plating and stripping process, preventing the lithium dendrites (Figure 10A).[106] However, Ishiguro et al. revealed higher interfacial resistance is in favor of long short-circuit period in the Ta-doped $Li_7La_3Zr_2O_{12}$ system. They believed that the grain boundaries phase at the Li/SE surface prevented the Li nucleation, although they contributed extra interfacial resistance.[60]
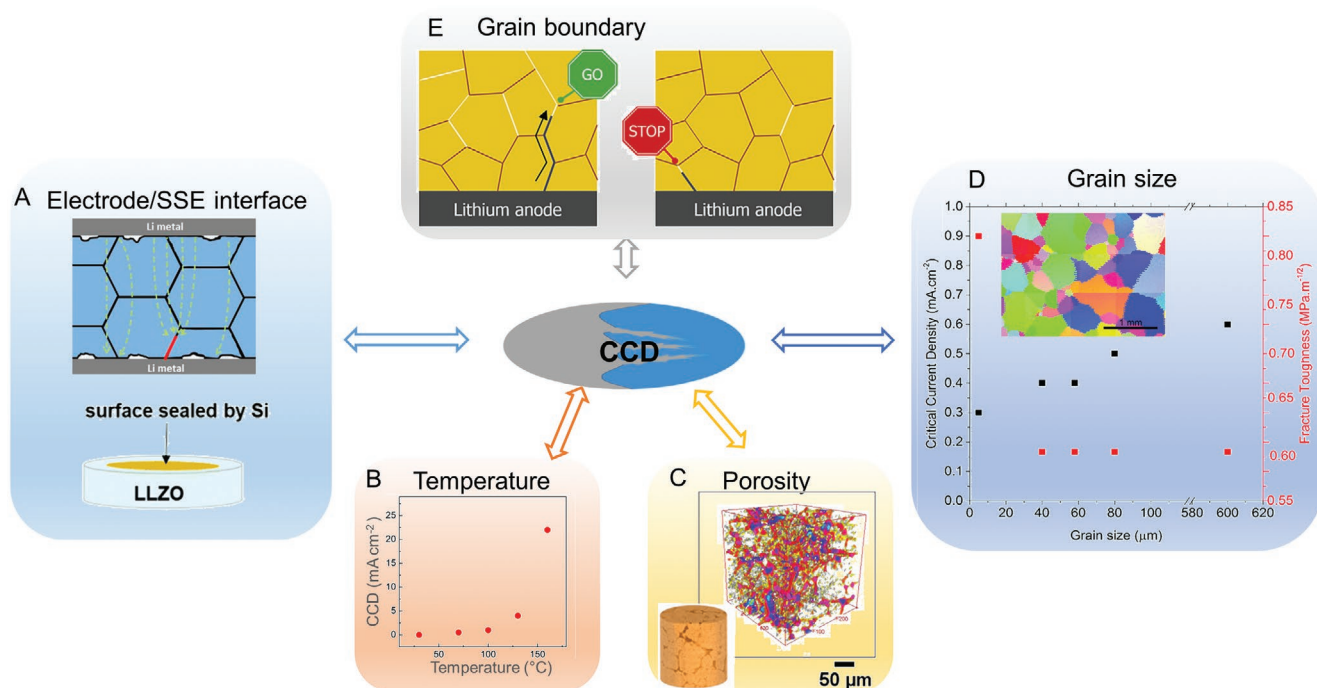
ADVANCED
SCIENCE NEWS
www.advancedsciencenews.com

ADVANCED
ENERGY
MATERIALS
www.advenergymat.de

Figure 10. Extrinsic and intrinsic affecting factors on determining CCD. A) Li/SE interface. Reproduced with permission.[66] Copyright 2016, American Chemical Society. Reproduced with permission.[106] Copyright 2018, Royal Society of Chemistry. B) Temperature. Reproduced with permission.[59] Copyright 2016, Elsevier B.V. C) Porosity. Reproduced with permission.[108] Copyright 2019, American Chemical Society. D) Grain size and shear modulus of SEs. Reproduced with permission.[110] Copyright 2017, Royal Society of Chemistry. E) Grain boundary. Reproduced with permission.[114] Copyright 2017, Elsevier B.V.

Temperature: High temperature can increase the CCD, and it is in favor of lithium dendrite prevention. Sharafi et al. studied the effect of temperature on CCD density of $Li_7La_3Zr_2O_{12}$.[59] The CCD increased with the test temperature, from 50 μA cm^{-1} to 14 mA cm^{-2}, as the temperature increased from 30 to 160 °C (Figure 10B). In addition, the CCD increased more obviously when the temperature reached the melting point. The continuous root-growth mechanism indicates that both Li^0 diffusion coefficient and creep rate increase with the increase of temperature, they decrease the driving force, thereby increasing the CCD. Sporadic bulk-plating mechanism suggests that the ionic conductivity of SE increases and the interfacial resistance decreases with the increase of temperature, they lead to a decreased overpotential in SE, thereby reducing the driving force and increasing the CCD.

Porosity: At first glance, high porosity should facilitate the lithium dendrite and decrease the CCD, as the lithium dendrite is likely to nucleate and grow in the pores. Ren et al. adjusted the relative density of Al-doped $Li_{6.75}La_3Zr_{1.75}Ta_{0.25}O_{12}$ by tuning the sintering temperature from 1050 to 1150 °C.[107] The results were consistent with the assumption that SEs with higher relative density exhibit longer short-circuit period. Lu et al. found the same trend with relative density in $Li_{6.5}La_3Zr_{1.5}Ta_{0.5}O_{12}$ when using Al_4Li_9 anode.[83] However, further dedications found that the CCD is not simply monotonous related to the relative density. Hatzell and co-workers[108] tuned the relative density of $Li_7La_3Zr_2O_{12}$ by adjusting the sintering temperature. Surprisingly, the CCD decreased with the increased relative density, which is in contrary to Ren's results.

X-ray tomography revealed that the large and connected pores, rather than small isolated pores, contributed to the lithium dendrites (Figure 10C). Although the further work of Ren et al. found the CCD increased with the relative density and decreased grain size in Ta-doped $Li_7La_3Zr_2O_{12}$, they agreed that the microstructure of the sintered body plays a more essential role in lithium dendrite prevention compared to the porosity alone.[109]

Shear Modulus: Despite of nucleation and growth mechanism, the compressive stress in SEs is considered as the major opposing force to nucleation and growth of lithium dendrite. The SEs with high shear modulus is expected to supply higher opposing force and increase the CCD.[7,86,89] However, the experiments did not show the inevitable relationship between shear modulus and CCD. Sharafi et al. prepared $Li_{6.25}Al_{0.25}La_3Zr_2O_{12}$ by hot-pressing method and tuned the hardness via adjusting the calcination temperature. The CCD did not change with decreasing hardness (Figure 10D). Therefore, Sharafi et al. believed that Monroe model is not applicable to the polycrystalline $Li_{6.25}Al_{0.25}La_3Zr_2O_{12}$.[110] In addition, comparing LLZO and Li_3PS_4, LLZO with a higher shear modulus exhibited a smaller CCD than that of Li_3PS_4, indicating the effect of shear modus to CCD is limited.[100]

Grain and Grain Boundary: Grain boundary plays an important role in lithium dendrite growth, as lithium nucleation and growth are related to the properties of grain boundary. The grain and grain boundary are highly related in the bulk SE, and their affects to the CCD are discussed in this section. However, the results are controversial.

**ADVANCED
SCIENCE NEWS**
www.advancedsciencenews.com

**ADVANCED
ENERGY
MATERIALS**
www.advenergymat.de

1) The number of grain boundaries. Theoretically, grain boundaries supply higher driving force and lower opposing force, therefore decreasing the CCD. Based on sporadic plating mechanism, Tian et al. pointed that the SEs with a finer grain size or higher volumetric percentage internal defect surface had a higher probability of isolated lithium nucleation.[100] Experimentally, hot-pressed $Li_{6.25}Al_{0.25}La_3Zr_2O_{12}$ with larger grain size and smaller number of grain boundaries per unit area exhibited larger CCD, because of reduced number of possible failure points (Figure 10D).[110] However, this observation is contrary to Ren's and Cheng's results, that the small particles contributed to high CCD.[107,111] In their report, small particles yielded a small interfacial resistance, making the grain boundary not the only parameter that affects the CCD.

2) Electrical properties of grain boundary. First, high ionic conductivity can reduce the driving force of lithium nucleation based on electrochemomechanical model, thereby increasing the CCD.[86] Most experiments demonstrated that high grain boundary conductivity is in favor of CCD. Cheng et al. showed that garnet electrolyte with higher grain boundary conductivity achieved by small particle construction can enlonger short-circuit period compared to that with smaller grain boundary conductivity.[111] Sudo et al. revealed a similar phenomenon in Al_2O_3 contained $Li_7La_3Zr_2O_{12}$. The composition with highest grain boundary conductivity exhibited the longest period before short circuit.[104] Although Pesci et al. revealed that Al dopant segregated at the grain boundaries and facilitated the nucleation and propagation of dendrites in $Li_{6.55}Al_{0.15}La_3Zr_2O_{12}$, resulting in a current density of 0.1 mA cm^{-2}.[112] Their observation still agreed that the high grain boundary conductivity can help to prevent lithium dendrite. In their report, $Li_{6.55}Ga_{0.15}La_3Zr_2O_{12}$ displayed a critical current density of 60% higher than that of $Li_{6.55}Al_{0.15}La_3Zr_2O_{12}$, because of clear grain boundary and higher Li$^+$ conductivity of the grain boundaries in $Li_{6.55}Ga_{0.15}La_3Zr_2O_{12}$.[113] However, Ishiguro et al. revealed that short-circuit period increased with the increase of grain boundary resistivity in Ta-doped $Li_7La_3Zr_2O_{12}$ system, which is contrast to the above results. They believed that low grain boundary conductivity slowed down the lithium dendrite growth, since the lithium dendrite grew through grain boundaries.[60] Second, higher electronic conductivity at grain boundaries decreases the required overpotential for lithium nucleation, therefore accelerating lithium dendrite and decreasing the CCD based on the sporadic plating mechanism. Song et al. introduced a thin layer of $LiAlO_2$ onto the grain boundaries of $Li_7La_{2.75}Ca_{0.25}Zr_{1.75}Nb_{0.25}O_{12}$ and increased the CCD, they suggested the reduced electronic conductivity at grain boundary should be the key reason.[102]

3) Microstructure of grain boundaries. Based on both continuous root-growth mechanism and sporadic bulk-plating mechanism, fracture strength of SE supplies the major opposing resistance to lithium dendrite. Basappa et al. introduced Li_2CO_3 and LiOH into $Li_{6.5}La_3Zr_{1.5}Ta_{0.5}O_{12}$ before sintering in order to modify the grain boundaries.[114] It is found that these Li_2CO_3 and LiOH not only filled out pores but also facilitated sintering. The modified garnets suppressed the dendrite growth along the grain boundaries and increased the CCD (Figure 10E). In addition, Xu et al. introduced Li_3PO_4 into the $Li_{6.5}La_3Zr_{1.5}Ta_{0.5}O_{12}$ along the grain boundaries. Li_3PO_4 reacted with fresh lithium dendrite and formed Li_3P, thereby suppressing the lithium dendrite growth and extending the short-circuit period.[115]

Although many efforts were made in order to reveal the individual contributions of interfacial structure, porosity, shear modulus, grain size, and grain boundary to lithium dendrite, the results have not come to an agreement. The major reason is the challenges in single variant control. The above variants are highly correlated with each other in SE. Even though, intimate Li/SE interface, well-sintered SEs with less connected pores, high ionic conductivity, and low electronic conductivity should be helpful in preventing lithium dendrite.

3. Cathode/Garnet Interface

Composite cathode containing cathode materials and SEs, is widely used in bulk-type ASSLBs. Different from the lithium/garnet interface, cathode/garnet interfaces include the interface within the composite cathode, and interface between cathode layer and garnet layer. Therefore, both the interfaces within the composite cathode and between the composite cathode layer and garnet layer are important. In addition, due to stiff nature of both cathode and SE, the interfacial engineering and interfacial phenomenon during cycling are much more different and complex.

3.1. Composition Optimization

For composite cathode, sufficient ionic and electronic conduction are required for electrochemical reaction. Bielefeld et al. applied percolation theory to study the individual contribution of composition, porosity, particle size, and electrode thickness to conduction.[116] They pointed out that the cathode materials contributed to electronic conduction, and SEs contributed to ionic conduction. An optimized composition range was 69–79 vol% of cathode material based on this pure microstructure model, in which no material characteristics except for particle's shape, size and overlap behavior were considered. Small particle size of cathode materials is desirable in terms of electronic conduction because they offer higher active surface areas and possibility to form percolating electronic clusters. In addition, small porosity is favorable in terms of conduction pathway, which leads to the necessity of manufacturing low porous electrodes.

3.2. Origin of Interfacial Resistance

Besides the composition optimization, interfacial building is another challenge. The interfacial resistance of composite cathode comes from insufficient particle contact, lattice mismatch, side reactions, and space charge effect (**Figure 11**). Space charge effect is significant in sulfide-based ASSLB, and its effect is limited in oxide-based ones when using oxide cathodes.[117–119]
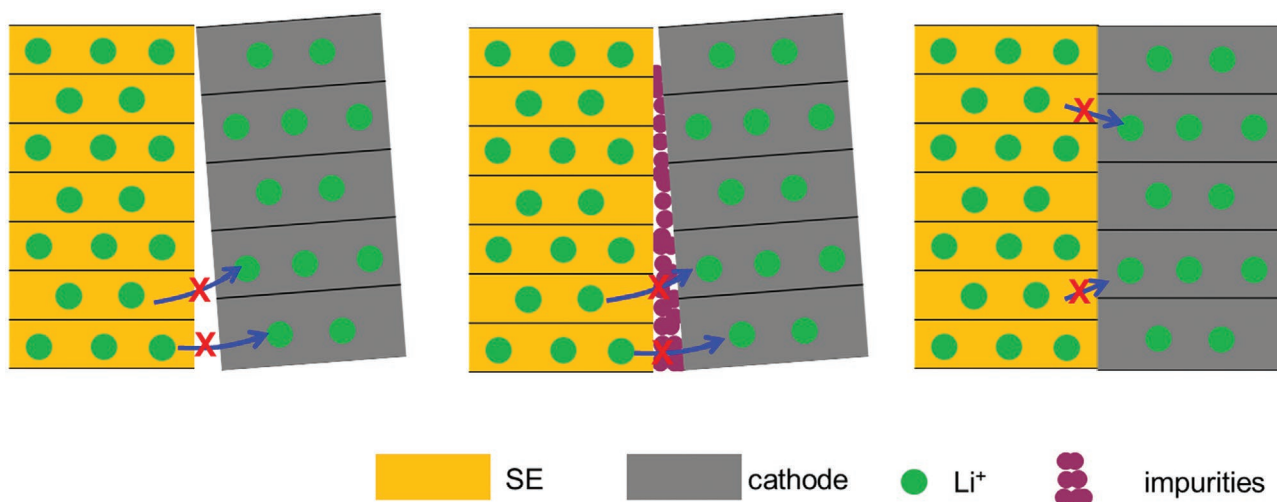
ADVANCED
SCIENCE NEWS
www.advancedsciencenews.com

ADVANCED
ENERGY
MATERIALS
www.advenergymat.de

Figure 11. Origin of interfacial resistance in cathode composite. A) Insufficient particle contact. B) Side reactions. C) Lattice mismatch.

3.2.1. Insufficient Particle Contact

Construction of cathode/SE interface is challenging because of solid–solid contact between cathodes and SEs. The gaps between cathode and SE block the lithium migration (Figure 11A). Broek et al. built a $Li_{6.25}Al_{0.25}La_3Zr_2O_{12}$ bilayer with one porous layer and one dense layer.[120] Although the contact areas were greatly increased because of 3D design, the interfacial resistance was still as high as 10 kΩ. Consequently, this 3D composite electrode exhibited a low specific capacity of 15 mAh g^{-1}, when it was operated at 95 °C. This means the simple loading of active materials onto SEs could not build an effective conduction due to insufficient particle contact at micro level. Two typical ways are effective in improving the particle contact and densification, i.e., higher pressure to increase the physical contact and remove the voids, and thermal annealing to fabricate the binding between particles by partial melting. Unlike relatively soft sulfide SE, high pressure is not applicable for stiff LLZO to improve physical contact because of the afraid of fracture. Instead, thermal treatment is generally employed in munufacturing cathode/garnet interface. Therefore, thermal stability between cathodes and SEs should be considered.

3.2.2. Thermal Reactions

Side reactions always happen in composite cathode between cathode and SE, including chemical reactions, electrochemical reactions and thermal reactions. The insulative reaction products exist between the particles, hindering the Li+ migration and introducing the extra interfacial resistance (Figure 11B). Thermal stability between cathode materials and garnet electrolytes is the prerequisite for thermal treatment. However, the absolute stability is hard to achieve. $LiCoO_2$ as cathode material is always used in ASSLBs, because of its high energy density and simple composition. The thermal reactions surely exist but the results are slightly different. Until now, three onset temperatures of thermal reaction were reported, i.e., 500, 700, and 1085 °C. Vardar et al. reported the $LiCoO_2$ reacted with Al-doped

$Li_7La_3Zr_2O_{12}$ at 500 °C, forming Li_2CO_3, $LaCoO_3$, and $La_3Zr_2O_7$. The interfacial resistance increased up to eight times than that of the as-deposited samples.[121] Park et al. predicted that upon heating the bilayer of $LiCoO_2$ and $Li_{6.02}Al_{0.2}La_3Zr_2O_{12}$ at 700 °C, a mutual diffusion as the interface was observed, resulting in a tetrahedral garnet phase due to Al diffusion.[122] Thermal characterization exhibited a small exothermal peak at about 700 °C and a large exothermal peak at 1085 °C upon calciantion of $LiCoO_2$ and $Li_{6.6}La_3Zr_{1.6}Ta_{0.4}O_{12}$.[123] Due to the relatively low sensitivity of XRD technique, the reaction at ≈700 °C is too gentle to be observed. XRD results revealed that severe phase reaction did not happen until 1085 °C, therafter, the impurites $LaCoO_3$, Li_2CoZrO_4, and $Li_3Zr_{0.18}Ta_{0.82}O_4$ were formed. Furthermore, a more complex layered system $Li(NiCoMn)_{1/3}O_2$ showed a worse thermal stability against LLZO. When sintered with LLZO at 600 °C, the Li tended to diffuse from the interface to $Li(NiCoMn)_{1/3}O_2$ to occupy the Ni vacancy, induced the decomposition of LLZO and the formation of $La_2Zr_2O_7$ and $LaNiO_3$ interfacial layer.[124] The decomposition of cathode, LLZO and formmation of insulative impurities impede the Li+ migration in cathode composite.

3.2.3. Lattice Mismatch

Lattice mismatch exists in polycrystals, and the typical one is the grain boundary resistance. In composite cathode, due to the different lattice parameter and lattice orientation of components, lattice mismatch exists and hinders the Li+ migration between grains (Figure 11C).

3.3. Postheat Treatment Method

3.3.1. Direct Thermal Annealing

Although thermal reaction could not be avoided, direct thermal annealing is still a typical and relative easy way for materials densification and binding by partial meling, therefore increasing the particle contact in microlevel. In afraid of thermal
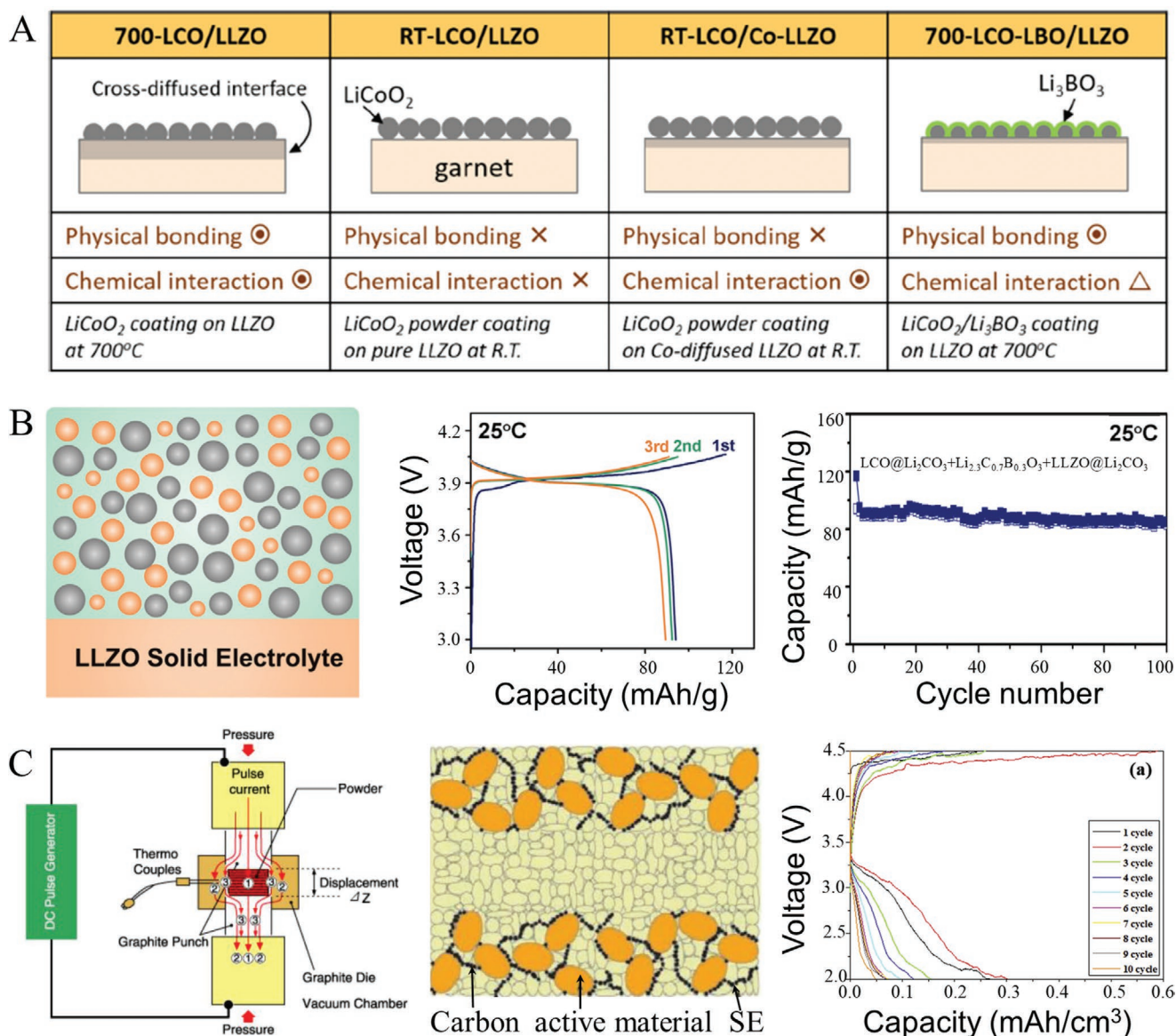
Figure 12. Interfacial engineering for solid-state cathode. A) Surface engineering between LiCoO$_2$ and garnet-type SEs. Reproduced with permission.[122] Copyright 2016, American Chemical Society. B) The electrochemical performance of ASSLBs using Li$_3$BO$_3$ as sintering additive and buffer layer. Reproduced with permission.[132] Copyright 2018, Elsevier B.V. C) Advanced sintering method (SPS) in constructing composite cathode and sandwich ASSLB. Reproduced with permission.[135] Copyright 2014, Elsevier B.V. Reproduced with permission.[136] Copyright 2017, Elsevier B.V.

reaction, thermal annealing is always undertaken at relatively low temperatures. Simply cosintering of LiCoO$_2$/garnets exhibited a good physical binding, thus yielding a discharge capacity of 35 mAh g^{-1} (**Figure 12A**).[122,125] Combination of 3D design and thermal treatment was employed to improve the contact area and Li kinetics at the interface, in order to enable ASSLB. Ren et al. prepared a bilayer Al-contained Li$_{6.75}$La$_3$Zr$_{1.75}$Ta$_{0.25}$O$_{12}$ pellet with one porous layer and on dense layer.[126] The LiCoO$_2$ solution was loaded into the porous layer by sol–gel method, and calcined at 600 °C to form the crystal LiCoO$_2$. However, the specific discharge capacity was still low, about 17 mAh g^{-1} when operated at 80 °C under a current density of 6.4 μA cm^{-2} (0.016 C). The poor electrochemical performance might be due

to the large interfacial resistance, about 10 kΩ cm^2. Wakayama and Kawai used a self-assembled block copolymer (BCP) structure as a template, the precursor for the cathode materials LiCoO$_2$ and garnet electrolyte Li$_7$La$_3$Zr$_2$O$_{12}$ were introduced and calcined at 750 °C in order to remove the BCP template and crystallize LiCoO$_2$ and Li$_7$La$_3$Zr$_2$O$_{12}$.[127] The nanostructured LiCoO$_2$ and Li$_7$La$_3$Zr$_2$O$_{12}$ composite cathode with the thickness of 25 μm was constructed, while the LiCoO$_2$ and Li$_7$La$_3$Zr$_2$O$_{12}$ were distributed homogeneously in the composite cathode. The obtained nanocomposite cathode, was constructed with polyethylene oxide doped with lithium bis(trifluoromethylsulfonyl) imide as separator. The composite cathode exhibited a specific discharge capacity of ≈135 mAh g^{-1} at the rate of 0.02 C, which

**ADVANCED
SCIENCE NEWS**

www.advancedsciencenews.com

**ADVANCED
ENERGY
MATERIALS**

www.advenergymat.de

might be due to the 3D conducting pathway. However, the interfacial resistance is still high, about 10 kΩ, resulting in a poor rate performance. Although 3D design increased the contact area, it accelerated the thermal reactions during annealing process at the same time.

3.3.2. Sintering Additive

Due to the high melting points (>1000 °C) of both garnets and cathode materials, direct thermal annealing of garnets and cathode materials is challenging in achieving excellent physical binding as well as avoiding chemical reaction, as discussed above. Increase of annealing temperature for better binding is not feasible because of accelerated thermal reactions at higher temperatures. Therefore, introduction of sintering additive during annealing process, not only can lower the annealing temperature, but also can mitigate the thermal reaction by avoiding the direct contact between cathodes and SEs.

The sintering additive used in cathode composite should exhibit low melting point, good stability with cathode and SE, high electronic conductivity, and/or ionic conductivity. Li_3BO_3 is a typical sintering aid used in oxide electrolyte, due to its relatively low melting point of ≈700 °C and moderate ionic conductivity of 2×10^{-6} S cm^{-1}.[128] Therefore, Li_3BO_3 plays roles as both SE and sintering aid. The single addition of Li_3BO_3 into the cathode as the SE exhibited a specific capacity of 0.6 mAh g^{-1}.[129] Ohta et al. applied Li_3BO_3 as both SEs and binding materials in electrode layer, the electrode layer was coated on the surface of $Li_{6.25}La_3Zr_{1.75}Nb_{0.25}O_{12}$ pellet by screen printing process, and postheat treated at 700 °C.[130] The constructed cathode/SE exhibited a total interfacial resistance of 230 Ω cm². The low interfacial resistance enabled the ASSLBs exhibiting a specific capacity of 85 mAh g^{-1}, keeping stable within 5 cycles at a rate of 0.05 C (10 μA cm^{-2}). The low interfacial resistance and good electrochemical properties of the ASSLB arisen from the good binding/contact between $LiCoO_2$ and $Li_{6.25}La_3Zr_{1.75}Nb_{0.25}O_{12}$ with the aid of Li_3BO_3. In the same way, Park et al. cosintered a mixture of $LiCoO_2$ and Li_3BO_3 on the surface of $Li_{6.02}Al_{0.2}La_3Zr_2O_{12}$ pellet, exhibiting a good electrochemical performance. The specific discharge capacity was 67.2 mAh g^{-1} and kept stable within 10 cycles.[122] It is proposed that the Li_3BO_3 not only enhanced the physical binding between $LiCoO_2$ and $Li_{6.02}Al_{0.2}La_3Zr_2O_{12}$, but also prevented the chemical interaction by obstructing the direct contact between $LiCoO_2$ and $Li_{6.02}Al_{0.2}La_3Zr_2O_{12}$ (Figure 12A).

Introduction of high conductive $Li_{6.8}La_{2.95}Ca_{0.05}Zr_{1.75}Nb_{0.25}O_{12}$ particles in cathode composite can enhance the Li$^+$ migration. In this case, Li_3BO_3 plays a role more like a binder rather than electroltye.[131] The mixture of $LiCoO_2$, Li_3BO_3, $Li_{6.8}La_{2.95}Ca_{0.05}Zr_{1.75}Nb_{0.25}O_{12}$ with a ratio of 42:35:23 (wt%) was pressed on the top of obtained $Li_{6.8}La_{2.95}Ca_{0.05}Zr_{1.75}Nb_{0.25}O_{12}$ pellet (1 mm), and cosintered at 790 °C. The obtained cell exhibited specific charge and discharge capacities of 98 and 78 mAh g^{-1}. Li_2CO_3 is generally formed on the surface of $LiCoO_2$ and garnets during storage, and it is dentrimental to the interfacial properteis. In addition,

Li_3BO_3 is likely to react with Li_2CO_3, forming a solid solution $Li_{2+x}C_{1-x}B_xO_3$. Han et al. ingeniously built the interface of the composite cathode by utilizing the reaction between Li_2CO_3 and Li_3BO_3. The constructed ASSLB exhibited a specific capacity of 94 mAh g^{-1} at 25 °C, with a good cycling performance (Figure 12B).[132]

In addition, the electrochemical perforamcne of ASSLBs are also limited by the slow electron migration. Liu et al. added In_2O_5Sn electronic conductive in complementary to the cathode materials, and Li_3BO_3 palyed roles as both SE and binder.[133] The fabricated ASSLBs exhited a discharge capacity of 101 mAh g^{-1} at a current density of 5 μA cm^{-2}. However, with the increase of cathode loading and thickness of cathode composite, the specific capacity decreased obviously due to the larger interfacial resistance in cathode composite.

Typically, introduction of sintering addtives can greatly improve the sinterability of composite cathode than direct thermal annealing. However, it is in an urgent need of a sintering additive with low melting point, high ionic conductivity, high electronic conductivity, strong binding ability, and good plasticity.

3.3.3. Spark Plasma Sintering

Spark plasma sintering (SPS), also known as field assisted sintering technique or pulsed electric current sitnering, is a fast sintering technique that can densify the powder compact near the theoretical density at lower sintering temperature compared to the convertional sitnering techniques.[134] In addtion, the internal heat generation mode facilates a very high heating and colling rate. Therefore, the sintering process is fast and the thermal reactions could be greatly alleviated.[135] Woo et al. employed SPS to construct the cathode composite.[136] Cathode materials $LiCoO_2$, SE ($Li_5La_3Ta_2O_{12}$), and multiwall carbon nanotube (MWCNT) as electronic additive were mixed togenther and sinteried. The optimized compostion (32:65:3) and sintering temperature (600–800 °C) were chosen for getting a continuous Li$^+$ and electron pathway and avoiding the reduction of $LiCoO_2$ by MWCNT. The cathode composite exhibited a specific discharge capacity of 91.96 mAh g^{-1} at a current density of 0.05 C when tested in liquid electrolyte. Amouphous LiPON was sputtered onto the top of composite cathode, in order to replace the applied liquid electrolyes. Then Li metal was deposited on the surface LiPON. The specific discharge capacity greatly droped to 0.3 mAh cm^{-2} at a current density of 0.05 C, when operated at 80 °C. The performance was mainly limited by the large ionic polariztion, which might be due to the low ionic conductivity of $Li_5La_3Ta_2O_{12}$, LiPON, and thick composite cathode (≈170 μm) (Figure 12C).

The bulk-type ASSLBs showed a much lower specific capacity than that of liquid batteries. The electrochemcial performance is limited not only by moderate lithium diffusivity at the cathode/electrolyte interface, but also in the SE if sintering additive is added. In addition, the thermal stability of composite cathode, including cathode materials, garnet electrolytes, electronic additive as well as sintering aids, needs special attention. The reported electrochemical performances of garnet-based ASSLBs are summarized in **Table 2**.

Table 2. The electrochemical performance of garnet-based ASSLBs.

Cathode composition	Temperature	Loading [mg cm^{-2}]	Current	Voltage range [V]	Capacity [mAh g^{-1}]	Number of cycle	References
LCO + 3DLLZO	80	N/A	6.4 µA cm^{-2}		17		Ren et al.[126]
LCO	RT	N/A	2 µA cm^{-2}	2.5–4.3	0.274	3	Kotobuki et al.[125]
LCO	50 °C	N/A	0.2 C	2.5–4.4	35	10	Park et al.[122]
LCO + LLZO		25 µm	0.02 C		135		Wakayama and Kawai[127]
LCO + Li$_3$BO$_3$	60 °C	N/A	14 µA cm^{-2}	2.5–4.2	0.6–7	5	Shoji et al.[129]
LCO + Li$_3$BO$_3$	25 °C	1.7	0.05 C	3.0–4.05	85	5	Ohta et al.[130]
LCO + Li$_3$BO$_3$	50 °C	N/A	0.2 C	2.5–4.4	67	10	Park et al.[122]
LCO + Li$_3$BO$_3$ + LLZO	RT	N/A	0.01 C	3.0–4.2	78	1	Ohta et al.[131]
LCO + Li$_3$BO$_3$ + In$_2$O$_5$Sn	RT	1.2	0.025 C	2.8–4.3	101	1	Liu et al.[133]
LCO@Li$_2$CO$_3$ + Li$_{2.3}$C$_{0.7}$B$_{0.3}$O$_3$ + LLZO@Li$_2$CO$_3$	25 °C	1	0.05	3.0–4.05	94	100	Han et al.[132]
LCO + MWCNT + LLTO	80 °C	N/A	0.05 C	2.0–4.5	0.3	10	Woo et al.[136]

3.4. Strain Accumulation and Mechanical Degradation during Cycling

The mechanical degradation is a serious issue in ASSLBs, as both electrode materials (nonlithium) and SEs are stiff in nature.[137] For most electrodes, the volume change will take place during lithiation and delithiation process (**Figure 13**A).[138] During lithiation process, the active material undergone crystal expansion. Mechanical degradation of SEs was caused by intercalation-induced expansion of electrode particles, within the constrain of a dense solid-state electrode. Bucci et al. studied the effects of materials properties to fracture by implementing a coupled electrochemomechanical model. As the particle stress-free strain increases, compressive stress develops in most of the microstructure. However, a few regions in proximity of the particles corner suffer from tensile stress (brown regions in the right contour plot in Figure 13B). This tension grows until large enough to initiate fractures in SE matrix, which is stage I. Thereafter, the cracks (marked with black lines) propagate in SEs at an approximately constant rate (stage II). Finally, the cracks propagate at a decreasing rate up to saturation. The propagation rate is highly dependent on the electrolyte elastic properties. A more compliant SE trends to deform more in the form of stretching and shearing in response to the volume change of electrode particles. An SE with stiffness closer to that of the active materials tends to develop higher compressive stress, but undergo lower tension. This results show that crack nucleation is delayed in tough SEs. The propagation rate and the final extension of cracks also decrease with the increasing SE stiffness (Figure 13C).[139] In composite electrode, SEs are responsible for binding active materials and establishing Li$^+$ conductions. However, the formation of microcracks within SEs are inevitable, resulting in a reduced effective lithium diffusivity and electrochemical performance (Figure 13D).[140] The in situ EIS indicated the change of interfacial resistance during charge and discharge process, while the bulk resistance of SE kept constant (Figure 13E). In addition, the microcracks were observed in composite cathode after cycles, demonstrating the above deductions (Figure 13F).[121,141–143]

As expected, the volume change of electrode materials induces the stress accumulation in SEs, and initiates the cracks. Actually, the composite cathode/garnet interfacial phenomenon is complex during cycling process. The interfacial phenomenon between cathode layer and garnet layer is different from which within composite electrodes. Even within composite cathodes, the structural changes are depth dependent. However, the current researches have not distinguished the structural evolution within the composite cathode and between the composite cathode layer and garnet layer. Assuming Li$^+$ diffusion is the rate-limited step in composite cathode, the electrochemical reaction should preferentially happen near the garnet side, then propagates into the composite cathode toward the current collector side. Therefore, it is reasonable to believe that the composite cathode near the garnet side exhibits a deeper charge–discharge, a larger volume change and a larger stress accumulation, resulting in a more serious mechanical degradation. The mechanical degradation is depth dependent and alleviated toward the current collector side. If electronic conduction is the rate-limited step in composite cathode, the mechanical degradation shows a contrary trend and is alleviated toward the garnet layer side. In addition, the overall volume change of composite cathode arising from the accumulation of individual volume change within the composite cathode would yield cracks even laminations between composite cathode layer and garnet layer (Figure 13F), exhibiting a more serious detriment to Li$^+$ migration. In short, the mechanical degradation takes places with propagation of cracks within the composite cathode and between the composite cathode and garnet, reduces the effective Li diffusivity in solid-state electrode, thus blocking the electrochemical performance.

Considering the strain-induced mechanical degradation and occurrence of cracks in stiff electrodes, few strategies are tentatively proposed to avoid/alleviate this degradation: 1) application of zero-strain cathode materials (not applicable for current cathode materials); 2) reducing the macrovolume change by using cathode composite showing opposite volume change; 3) redistributing the strain in composite cathode by using small cathode particles; 4) introduction of soft buffer layer to absorb the strain accumulation; 5) strengthening the binding between cathode materials and SEs. These strategies are expected to reduce the
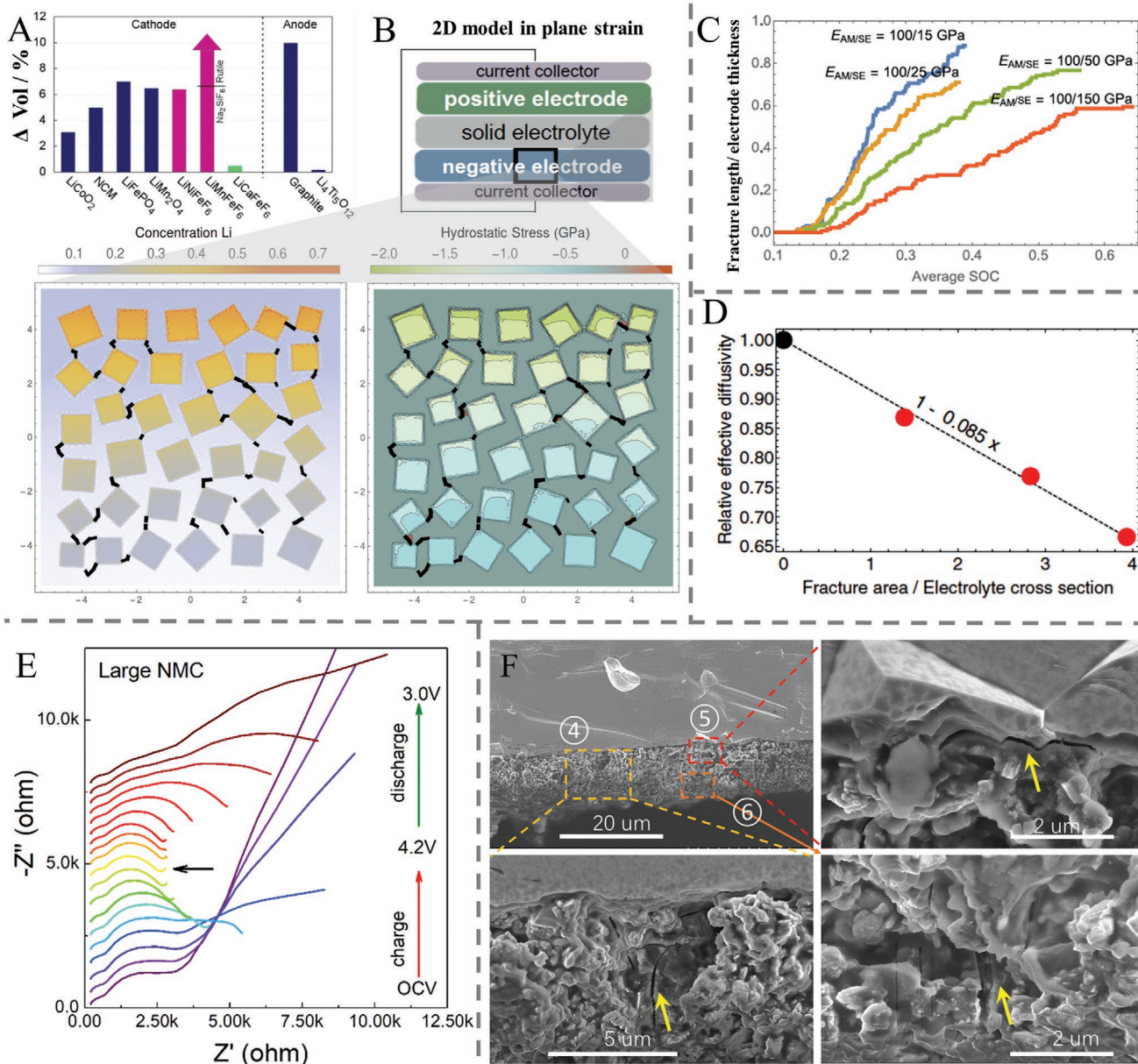
**ADVANCED
SCIENCE NEWS**
www.advancedsciencenews.com

**ADVANCED
ENERGY
MATERIALS**
www.advenergymat.de

Figure 13. Volume change induced strain accumulation and associated mechanical and electrical properties. A) Volume change of electrode materials during charge and discharge, Reproduced with permission.[138] Copyright 2017, Elsevier B.V. B) Strain accumulation in SSLBs during lithiation process. Reproduced with permission.[139] Copyright 2017, Royal Society of Chemistry. C) Mechanical fracture in electrode of SSLBs. Reproduced with permission.[139] Copyright 2017, Royal Society of Chemistry. D) Effective diffusivity with the mechanical fracture. Reproduced with permission.[140] Copyright 2017, American Chemical Society. E) In situ characterization of impedance evolution in SSLBs. Reproduced with permission.[141] Copyright 2019, American Chemical Society. F) Microcracks observed in composite cathode after cycles. Reproduced with permission.[141] Copyright 2019, American Chemical Society.

strain initiation, absorb the strain via soft materials and increase the resistance to the strain, thereby depressing the formation of cracks and maintaining the mechanical morphologies.

4. Conclusion and Prospective

In conclusion, we reviewed and summarized the recent development of interfacial issues in garnet-type ASSLBs, including interfacial building of garnets with Li metal and cathode materials, as well as the subsequent interfacial degradation/failure during cycling process. In anode side, the interfacial resistance arises from the surface contaminated Li_2CO_3 from the air, ineffective contact, and side reactions between Li and garnets. Strategies such as surface cleaning, Li annealing, external press, and introduction of artificial interlayer are applied to reduce the interfacial resistance. Even an excellent initial Li/garnet interface is built, the inhomogeneous stripping and

plating upon charge and discharge will also deteriorate the interface, increase the interfacial resistance and facilitate the lithium dendrite. Two mechanisms are proposed to explain the dendrite growth, including the continuous root-growth mechanism and sporadic bulk-plating mechanism, but still in controversial. The CCD is used to evaluate the dendrite resistance of SE. It is found the uniform Li/garnet interface, dense garnets with less connected pores, high ionic conductivity, and low electronic conductivity are helpful in preventing lithium dendrite. In cathode side, the interfacial resistance arises from the poor physical contacts, side reactions, and lattice mismatch between garnets and cathodes. Strategies including 3D design, postconventional sintering, addition of sintering additive, and spark plasma sintering techniques are employed to increase the effective contacts, facilitate the Li$^+$ kinetics and alleviate the side reactions between garnets and cathodes, therefore reducing the interfacial resistance. However, the volume change of active materials during subsequent charge and discharge process causes the strain initiation and accumulation in stiff electrode, and triggers the formation of cracks and mechanical degradation, therefore deteriorating the electrochemical performance.

The interfacial building has received great attention during the last decades because of its significances in determining the performance of ASSLBs. However, several challenges still exist, and the following aspects are worth to note: 1) although the resistance of as-built Li and garnets interface has been reduced to several tens of ohms, the inhomogeneous stripping and plating during subsequent charge–discharge process will deteriorate the interfacial morphology, reduce the effective contact area, and increase the interfacial resistance. Strategies need to be designed to maintain the effective contacts during cycling process, especially at high current densities. 2) Lithium dendrites are not avoided in ASSLBs as expected. A convincing fundamental understanding of growth mechanism of lithium dendrite and the associated affect factors are required. Optimized properties of garnets and their interfaces to Li are required in order to prevent or slow down the lithium dendrite growth. 3) The interfacial properties between cathodes and garnets are still not satisfied, and how to build a perfect interface is challenging due to their stiff nature. The origin of interfacial resistance needs to be identified, and the advanced sintering techniques and special interfacial design need further development for improving the Li$^+$ dynamics between garnets and cathode materials. 4) Interfacial degradation in stiff composite cathode should be dedicated on. The relationship between volume change of active materials, strain initiation/accumulation, morphology degradation, impedance evolution, and electrochemical performance should be specified. Strategies need to develop in order to maintain a stable and recoverable morphology in stiff cathode during cycling process for long lifetime of ASSLBs. Introduction of a soft buffer layer should be a possible choice to alleviate the strain accumulation in stiff electrodes. 5) In situ and operando characterizations are expected in order to provide insights into the morphology evolution and transport phenomenon occurring at both the anodic and cathodic interfaces, guiding the rational design of interfacial structure and building methodology for garnet-based ASSLBs.

Conflict of Interest

The authors declare no conflict of interest.

[1] S. S. Zhang, *J. Power Sources* **2006**, *162*, 1379.
[2] Z. Chen, K. Amine, *Electrochem. Commun.* **2007**, *9*, 703.
[3] X. Feng, M. Ouyang, X. Liu, L. Lu, Y. Xia, X. He, *Energy Storage Mater.* **2018**, *10*, 246.
[4] V. Ruiz, A. Pfrang, A. Kriston, N. Omar, P. Van den Bossche, L. Boon-Brett, *Renewable Sustainable Energy Rev.* **2018**, *81*, 1427.
[5] T. Inoue, K. Mukai, *ACS Appl. Mater. Interfaces* **2017**, *9*, 1507.
[6] X.-B. Cheng, R. Zhang, C.-Z. Zhao, Q. Zhang, *Chem. Rev.* **2017**, *117*, 10403.
[7] C. Monroe, J. Newman, *J. Electrochem. Soc.* **2005**, *152*, A396.
[8] S. Yu, R. D. Schmidt, R. Garcia-Mendez, E. Herbert, N. J. Dudney, J. B. Wolfenstine, J. Sakamoto, D. J. Siegel, *Chem. Mater.* **2016**, *28*, 197.
[9] T. Thompson, S. Yu, L. Williams, R. D. Schmidt, R. Garcia-Mendez, J. Wolfenstine, J. L. Allen, E. Kioupakis, D. J. Siegel, J. Sakamoto, *ACS Energy Lett.* **2017**, *2*, 462.
[10] W. D. Richards, L. J. Miara, Y. Wang, J. C. Kim, G. Ceder, *Chem. Mater.* **2016**, *28*, 266.
[11] G. Oh, M. Hirayama, O. Kwon, K. Suzuki, R. Kanno, *Chem. Mater.* **2016**, *28*, 2634.
[12] P. Knauth, *Solid State Ionics* **2009**, *180*, 911.
[13] R. Chen, W. Qu, X. Guo, L. Li, F. Wu, *Mater. Horiz.* **2016**, *3*, 487.
[14] Y. Zhu, X. He, Y. Mo, *J. Mater. Chem. A* **2016**, *4*, 3253.
[15] F. Han, Y. Zhu, X. He, Y. Mo, C. Wang, *Adv. Energy Mater.* **2016**, *6*, 1501590.
[16] E. J. Cussen, *J. Mater. Chem.* **2010**, *20*, 5167.
[17] M. P. O'Callaghan, D. R. Lynham, E. J. Cussen, G. Z. Chen, *Chem. Mater.* **2006**, *18*, 4681.
[18] E. J. Cussen, T. W. S. Yip, G. O'Neill, M. P. O'Callaghan, *J. Solid State Chem.* **2011**, *184*, 470.
[19] R. Murugan, V. Thangadurai, W. Weppner, *J. Electrochem. Soc.* **2008**, *155*, A90.
[20] R. Murugan, V. Thangadurai, W. Weppner, *Angew. Chem., Int. Ed.* **2007**, *46*, 7778.

[21] J. Percival, E. Kendrick, R. I. Smith, P. R. Slater, *Dalton Trans.* **2009**, *26*, 5177.

[22] A. Gupta, R. Murugan, M. P. Paranthaman, Z. Bi, C. A. Bridges, M. Nakanishi, A. P. Sokolov, K. S. Han, E. W. Hagaman, H. Xie, C. B. Mullins, J. B. Goodenough, *J. Power Sources* **2012**, *209*, 184.

[23] X. Huang, C. Liu, Y. Lu, T. Xiu, J. Jin, M. E. Badding, Z. Wen, *J. Power Sources* **2018**, *382*, 190.

[24] J. Awaka, A. Takashima, K. Kataoka, N. Kijima, Y. Idemoto, J. Akimoto, *Chem. Lett.* **2011**, *40*, 60.

[25] J. Han, J. Zhu, Y. Li, X. Yu, S. Wang, G. Wu, X. Hui, S. C. Vogel, F. Izumi, K. Momma, Y. Kawamura, Y. Huang, J. B. Goodenough, Y. Zhao, *Chem. Commun.* **2012**, *48*, 9840.

[26] D. Wang, G. Zhong, W. K. Pang, Z. Guo, Y. Li, M. J. McDonald, J. Mi, R. Fu, Y. Yang, *Chem. Mater.* **2015**, *27*, 6650.

[27] L. Cheng, E. J. Crumlin, W. Chen, R. Qiao, H. Hou, S. F. Lux, V. Zorba, R. Russo, R. Kostecki, Z. Liu, K. Persson, W. Yang, J. Cabana, T. Richardson, G. Chen, M. Doeff, *Phys. Chem. Chem. Phys.* **2014**, *16*, 18294.

[28] A. Sharafi, M. N. Yu, M. Lee, C. Ma, H. M. Meyer, J. Nanda, M. Chi, D. J. Siegel, J. Sakamoto, *J. Mater. Chem. A* **2017**, *5*, 13475.

[29] C. Ma, E. Rangasamy, C. Liang, J. Sakamoto, K. L. More, M. Chi, *Angew. Chem., Int. Ed.* **2015**, *54*, 129.

[30] L. Truong, M. Howard, O. Clemens, K. S. Knight, P. R. Slater, V. Thangudurai, *J. Mater. Chem. A* **2013**, *1*, 13469.

[31] L. Cheng, M. Liu, A. Mehta, H. Xin, F. Lin, K. Persson, G. Chen, E. J. Crumlin, M. Doeff, *ACS Appl. Energy Mater.* **2018**, *1*, 7244.

[32] Z. Zhang, Y. Shao, B. Lotsch, Y.-S. Hu, H. Li, J. Janek, L. F. Nazar, C. Nan, J. Maier, M. Armand, L. Chen, *Energy Environ. Sci.* **2018**, *11*, 1945.

[33] V. Thangadurai, S. Narayanman, D. Pinzaru, *Chem. Soc. Rev.* **2014**, *43*, 4714.

[34] C. Cao, Z.-B. Li, X.-L. Wang, X.-B. Zhao, W.-Q. Han, *Front. Energy Res.* **2014**, *2*, 25.

[35] S. Teng, J. Tan, A. Tiwari, *Curr. Opin. Solid State Mater. Sci.* **2014**, *18*, 29.

[36] D. Wang, G. Zhong, O. Dolotko, Y. Li, M. J. McDonald, J. Mi, R. Fu, Y. Yang, *J. Mater. Chem. A* **2014**, *2*, 20271.

[37] N. Zhao, W. Khokhar, Z. Bi, C. Shi, X. Guo, L.-Z. Fan, C.-W. Nan, *Joule* **2019**, *3*, 1190.

[38] S. A. Pervez, M. A. Cambaz, V. Thangadurai, M. Fichtner, *ACS Appl. Mater. Interfaces* **2019**, *11*, 22029.

[39] Q. Liu, Z. Geng, C. Han, Y. Fu, S. Li, Y.-B. He, F. Kang, B. Li, *J. Power Sources* **2018**, *389*, 120.

[40] A. Manthiram, X. Yu, S. Wang, *Nat. Rev. Mater.* **2017**, *2*, 16103.

[41] J. Dai, C. Yang, C. Wang, G. Pastel, L. Hu, *Adv. Mater.* **2018**, *30*, 1802068.

[42] A. J. Samson, K. Hofstetter, S. Bag, V. Thangadurai, *Energy Environ. Sci.* **2019**, *12*, 2957.

[43] C. Sun, Y. Ruan, W. Zha, W. Li, M. Cai, Z. Wen, *Mater. Horiz.* **2020**, *7*, 1667.

[44] Y. Zhu, X. He, Y. Mo, *ACS Appl. Mater. Interfaces* **2015**, *7*, 23685.

[45] S. Wenzel, T. Leichtweiss, D. Kruger, J. Sann, J. Janek, *Solid State Ionics* **2015**, *278*, 98.

[46] H. E. Shinawi, J. Janek, *J. Power Sources* **2013**, *225*, 13.

[47] J. Wolfenstine, J. L. Allen, J. Read, J. Sakamoto, *J. Mater. Sci.* **2013**, *48*, 5846.

[48] C. Wang, Y. Gong, B. Liu, K. Fu, Y. Yao, E. Hitz, Y. Li, J. Dai, S. Xu, W. Luo, E. D. Wachsman, L. Hu, *Nano Lett.* **2017**, *17*, 565.

[49] S. Ohta, T. Kobayashi, T. Asaoka, *J. Power Sources* **2011**, *196*, 3342.

[50] M. Fingerle, C. Loho, T. Ferber, H. Hahn, R. Hausbrand, *J. Power Sources* **2017**, *366*, 72.

[51] C. Ma, Y. Chen, K. Yin, J. Luo, A. Sharafi, J. Sakamoto, J. Li, K. L. More, N. J. Dudney, M. Chi, *Nano Lett.* **2016**, *16*, 7030.

[52] X. Han, Y. Gong, K. Fu, X. He, G. T. Hitz, J. Dai, A. Pearse, B. Liu, H. Wang, G. Rubloff, Y. Mo, V. Thangadurai, E. D. Wachsman, L. Hu, *Nat. Mater.* **2017**, *16*, 572.

[53] Y. Zhu, J. G. Connell, S. Tepavcevic, P. Zapol, R. Garcia-Mendez, J. T. N, J. Sakamoto, B. J. Ingram, L. A. Curtiss, J. W. Freeland, D. D. Fong, N. M. Markovic, *Adv. Energy Mater.* **2019**, *9*, 1803440.

[54] H. Zheng, S. Wu, R. Tian, Z. Xu, H. Zhu, H. Duan, H. Liu, *Adv. Funct. Mater.* **2019**, *29*, 1906189.

[55] H. Huo, J. Luo, V. Thangadurai, X. Guo, C.-W. Nan, X. Sun, *ACS Energy Lett.* **2020**, *5*, 252.

[56] A. Sharafi, E. Kazyak, A. L. Davis, S. Yu, T. Thompson, D. J. Siegel, N. P. Dasgupta, J. Sakamoto, *Chem. Mater.* **2017**, *29*, 7961.

[57] T. Krauskopf, H. Hartmann, W. G. Zeier, J. Janek, *ACS Appl. Mater. Interfaces* **2019**, *11*, 14463.

[58] F. Yonemoto, A. Nishimura, M. Motoyama, N. Tsuchimine, S. Kobayashi, Y. Iriyama, *J. Power Sources* **2017**, *343*, 207.

[59] A. Sharafi, H. M. Meyer, J. Nanda, J. Wolfenstine, J. Sakamoto, *J. Power Sources* **2016**, *302*, 135.

[60] K. Ishiguro, H. Nemori, S. Sunahiro, Y. Nakata, R. Sudo, M. Matsui, Y. Takeda, O. Yamamoto, N. Imanishi, *J. Electtrochem. Soc.* **2014**, *161*, A668.

[61] H. Huo, Y. Chen, N. Zhao, X. Lin, J. Luo, X. Yang, Y. Liu, X. Guo, X. Sun, *Nano Energy* **2019**, *61*, 119.

[62] Y. Ruan, Y. Lu, X. Huang, J. Su, C. Sun, J. Jin, Z. Wen, *J. Mater. Chem. A* **2019**, *7*, 14565.

[63] J.-F. Wu, B.-W. Pu, D. Wang, S.-Q. Shi, N. Zhao, X. Guo, X. Guo, *ACS Appl. Mater. Interfaces* **2019**, *11*, 898.

[64] Y. Li, X. Chen, A. Dolocan, Z. Cui, S. Xin, L. Xue, H. Xu, K. Park, J. Am. Chem. Soc. **2018**, *140*, 6448.

[65] P. G. Slade, *Electrical Contacts: Principles and Applications*, CRC Press, Boca Raton, FL **2017**.

[66] C.-L. Tsai, V. Roddatis, C. V. Chandran, Q. Ma, S. Uhlenbruck, M. Bram, P. Heitjans, O. Guilon, *ACS Appl. Mater. Interfaces* **2016**, *8*, 10617.

[67] W. Feng, X. Dong, P. Li, Y. Wang, Y. Xia, *J. Power Sources* **2019**, *419*, 91.

[68] K. K. Fu, Y. Gong, B. Liu, Y. Zhu, S. Xu, Y. Yao, W. Luo, C. Wang, S. D. Lacey, J. Dai, *Sci. Adv.* **2017**, *3*, e1601659.

[69] J. Duan, L. Huang, T. Wang, Y. Huang, H. Fu, W. Wu, W. Luo, Y. Huang, *Adv. Funct. Mater.* **2020**, *30*, 1908701.

[70] W. Luo, Y. Gong, Y. Zhu, Y. Li, Y. Yao, Y. Zhang, K. K. Fu, G. Pastel, C. F. Lin, Y. Mo, *Adv. Mater.* **2017**, *29*, 1606042.

[71] W. Luo, Y. Gong, Y. Zhu, K. K. Fu, J. Dai, S. D. Lacey, C. Wang, B. Liu, X. Han, Y. Mo, *J. Am. Chem. Soc.* **2016**, *138*, 12258.

[72] J. Duan, W. Wu, A. M. Nolan, T. Wang, J. Wen, C. Hu, Y. Mo, W. Luo, Y. Huang, *Adv. Mater.* **2019**, *31*, 1807243.

[73] Y. Shao, H. Wang, Y. Lu, D. Wang, B. Zheng, J. Zhu, Z. Gong, Y. Hu, X. Guo, H. Li, X. Huang, Y. Yang, C.-W. Nan, L. Chen, *ACS Energy Lett.* **2018**, *3*, 1212.

[74] W. Feng, X. Dong, X. Zhang, Z. Lai, P. Li, C. Wang, Y. Wang, Y. Xia, *Angew. Chem., Int. Ed.* **2020**, *59*, 5346.

[75] Y. Chen, M. He, N. Zhao, J. Fu, H. Huo, T. Zhang, Y. Li, F. Xu, X. Guo, *J. Power Sources* **2019**, *420*, 15.

[76] B. Hu, W. Yu, B. Xu, X. Zhang, T. Liu, Y. Shen, Y.-H. Lin, C.-W. Nan, L. Li, *ACS Appl. Mater. Interfaces* **2019**, *11*, 34939.

[77] J. Fu, P. Yu, N. Zhang, G. Ren, S. Zheng, W. Huang, X. Long, H. Li, X. Liu, *Energy Environ. Sci.* **2019**, *12*, 1404.

[78] M. Cai, Y. Lu, J. Su, Y. Ruan, C. Chen, B. V. R. Chowdari, Z. Wen, *ACS Appl. Mater. Interfaces* **2019**, *11*, 35030.

[79] H. Huo, Y. Chen, R. Li, N. Zhao, J. Luo, J. G. P. da Siva, R. Mucke, P. Kaghazchi, X. Guo, X. Sun, *Energy Environ. Sci.* **2020**, *13*, 127.

[80] W. Feng, X. Dong, Z. Lai, X. Zhang, Y. Wang, C. Wang, J. Luo, Y. Xia, *ACS Energy Lett.* **2019**, *4*, 1725.

[81] R. H. Basappa, T. Ito, H. Yamada, *J. Electrochem. Soc.* **2017**, *164*, A666.

[82] M. J. Wang, R. Choudhury, J. Sakamoto, *Joule* **2019**, *3*, 2165.

[83] Y. Lu, X. Huang, Y. Ruan, Q. Wang, R. Kun, J. Yang, Z. Wen, *J. Mater. Chem. A* **2018**, *6*, 18853.

[84] C. Yang, H. Xie, W. Ping, K. Fu, B. Liu, J. Rao, Q. Dai, C. Wang, G. Pastel, L. Hu, *Adv. Mater.* **2019**, *31*, 1804815.

[85] T. Kraukopf, B. Mogwitz, C. Rosenbach, W. G. Zeier, J. Janek, *Adv. Energy Mater.* **2019**, *9*, 1902568.

[86] R. Raj, J. Wolfenstine, *J. Power Sources* **2017**, *343*, 119.

[87] K. Ishiguro, Y. Nakata, M. Matsui, I. Uechi, Y. Takeda, O. Yamamoto, N. Imanishi, *J. Electrochem. Soc.* **2013**, *160*, A1690.

[88] F. Han, A. S. Westover, J. Yue, X. Fan, F. Wang, M. Chi, D. N. Leonard, N. J. Dudney, H. Wang, C. Wang, *Nat. Energy* **2019**, *4*, 187.

[89] T. Krauskopf, R. Dippel, H. Hartmann, K. Peppler, B. Mogwitz, F. H. Richter, W. G. Zeier, J. Janek, *Joule* **2019**, *3*, 2030.

[90] L. E. Marbella, S. Zekoll, J. Kasemchainan, S. P. Emge, P. G. Bruce, C. P. Grey, *Chem. Mater.* **2019**, *31*, 2762.

[91] E. J. Cheng, A. Sharafi, J. Sakamoto, *Electrochim. Acta* **2017**, *223*, 85.

[92] F. Shen, M. B. Dixit, X. Xiao, K. B. Hatzell, *ACS Energy Lett.* **2018**, *3*, 1056.

[93] L. Porz, T. Swamy, B. W. Sheldon, D. Rettenwander, T. Fromling, H. L. Thaman, S. Berendts, R. Uecker, W. C. Carter, Y.-M. Chiang, *Adv. Energy Mater.* **2017**, *7*, 1701003.

[94] M. Wang, J. B. Wolfenstine, J. Sakamoto, *Electrochim. Acta* **2019**, *296*, 842.

[95] S. Kim, C. Jung, H. Kim, K. E. Thomas-Alyea, G. Yoon, B. Kim, M. E. Badding, Z. Song, J. Chang, J. Kim, D. Im, K. Kang, *Adv. Energy Mater.* **2020**, *10*, 1903993.

[96] L. Zhang, T. Yang, C. Du, Q. Liu, Y. Tang, J. Zhao, B. Wang, T. Chen, Y. Sun, P. Jia, H. Li, L. Geng, J. Chen, H. Ye, Z. Wang, Y. Li, H. Sun, X. Li, Q. Dai, Y. Tang, Q. Peng, T. Shen, S. Zhang, T. Zhu, J. Huang, *Nat. Nanotechnol.* **2020**, *15*, 94.

[97] S. Yu, D. J. Siegel, *ACS Appl. Mater. Interfaces* **2018**, *10*, 38151.

[98] F. Aguesse, W. Manalastas, L. Buannic, J. M. Lopez del Amo, G. Singh, A. Llordes, J. Kilner, *ACS Appl. Mater. Interfaces* **2017**, *9*, 3808.

[99] H.-K. Tian, B. Xu, Y. Qi, *J. Power Sources* **2018**, *392*, 79.

[100] H.-K. Tian, Z. Liu, Y. Ji, L.-Q. Chen, Y. Qi, *Chem. Mater.* **2019**, *31*, 7351.

[101] W. Manalastas Jr., J. Rikarte, R. J. Chater, R. Brugge, A. Aguadero, L. Buannic, A. Llordes, F. Aguesse, J. Kilner, *J. Power Sources* **2019**, *412*, 287.

[102] Y. Song, L. Yang, W. Zhao, Z. Wang, Y. Zhao, Z. Wang, Q. Zhao, H. Liu, F. Pan, *Adv. Energy Mater.* **2019**, *9*, 1900671.

[103] F. Flatscher, M. Rhilipp, S. Ganschow, H. M. R. Wilkening, D. Rettenwander, *J. Mater. Chem. A* **2020**, *8*, 15782.

[104] R. Sudo, Y. Nakata, K. Ishiguro, M. Matsui, A. Hirano, Y. Takeda, O. Yamamoto, N. Imanishi, *Solid State Ionics* **2014**, *262*, 151.

[105] T. Krauskopf, R. Dippel, H. Hartmann, K. Peppler, B. Mogwitz, F. H. Richter, W. G. Zeier, J. Janek, *Joule* **2019**, *3*, 2030.

[106] B. Wu, S. Wang, J. Lochala, D. Desrochers, B. Liu, W. Zhang, J. Yang, J. Xiao, *Energy Environ. Sci.* **2018**, *11*, 1803.

[107] Y. Ren, Y. Shen, Y. Lin, C.-W. Nan, *Electrochem. Commun.* **2015**, *57*, 27.

[108] M. B. Dixit, M. Regala, F. Shen, X. Xiao, K. B. Hatzell, *ACS Appl. Mater. Interfaces* **2019**, *11*, 2022.

[109] Y. Ren, Y. Shen, Y. Lin, C.-W. Nan, *ACS Appl. Mater. Interfaces* **2019**, *11*, 5928.

[110] A. Sharafi, C. G. Haslam, R. D. Kerns, J. Wolfenstine, J. Sakamoto, *J. Mater. Chem. A* **2017**, *5*, 21491.

[111] L. Cheng, W. Chen, M. Kunz, K. Persson, N. Tamura, G. Chen, M. Doeff, *ACS Appl. Mater. Interfaces* **2015**, *7*, 2073.

[112] F. M. Pesci, R. H. Brugge, A. K. Ola Hekselman, A. Cavallaro, R. J. Chater, A. Aguadero, *J. Mater. Chem. A* **2018**, *6*, 19817.

[113] M. D. Tikekar, S. Chouodhury, Z. Tu, L. A. Archer, *Nat. Energy* **2016**, *1*, 16114.

[114] R. H. Basappa, T. Ito, T. Morimura, R. Bekarevich, K. Mitsuishi, H. Yamada, *J. Power Sources* **2017**, *363*, 145.

[115] B. Xu, W. Li, H. Duan, H. Wang, Y. Guo, H. Li, H. Liu, *J. Power Sources* **2017**, *354*, 68.

[116] A. Bielefeld, D. A. Weber, J. Janek, *J. Phys. Chem. C* **2019**, *123*, 1626.

[117] A. C. Luntz, J. Voss, K. Reuter, *J. Phys. Chem. Lett.* **2015**, *6*, 4599.

[118] B. Wu, S. Wang, W. J. EvansIV, D. Z. Deng, J. Yang, J. Xiao, *J. Mater. Chem. A* **2016**, *4*, 15266.

[119] K. Takada, T. Ohno, N. Ohta, T. Ohnishi, Y. Tanaka, *ACS Energy Lett.* **2018**, *3*, 98.

[120] J. V. D. Broek, S. Afyon, J. L. M. Rupp, *Adv. Energy Mater.* **2016**, *6*, 1600736.

[121] G. Vardar, W. J. Bowman, Q. Lu, J. Wang, R. J. Chater, A. Aguadero, R. Seibert, J. Terry, A. hunt, I. Waluyo, D. D. Fong, A. Jarry, E. J. Crumlin, S. L. Hellstrom, Y.-M. Chiang, B. Yildiz, *Chem. Mater.* **2018**, *30*, 6259.

[122] K. Park, B. C. Yu, J.-W. Jung, Y. Li, W. Zhou, H. Gao, S. Son, J. B. Goodenough, *Chem. Mater.* **2016**, *28*, 8051.

[123] S. Uhlenbruck, J. Dornseiffer, S. Lobe, C. Dellen, C.-L. Tsai, B. Gotzen, D. Sebold, M. Finsterbusch, O. Guillon, *J. Electroceram.* **2017**, *38*, 197.

[124] N. Zhang, X. Long, Z. Wang, F. H. P. Yu, J. Fu, G. Ren, Y. Wu, S. Zheng, W. Huang, C. Wang, H. Li, X. Liu, *ACS Energy Mater.* **2018**, *1*, 5968.

[125] M. Kotobuki, H. Munakata, K. Kanamura, Y. Sato, T. Yoshida, *J. Electrochem. Soc.* **2010**, *157*, A1076.

[126] Y. Ren, T. Liu, Y. Shen, Y. Lin, C.-W. Nan, *Ionics* **2017**, *23*, 2521.

[127] H. Wakayama, Y. Kawai, *J. Mater. Chem. A* **2017**, *5*, 18816.

[128] R. D. Shannon, B. E. Taylor, A. D. English, T. Berzins, *Electrochim. Acta* **1977**, *22*, 783.

[129] M. Shoji, H. Munakata, K. Kanamura, *Front. Energy Res.* **2016**, *4*, 32.

[130] S. Ohta, S. Komagata, J. Seki, T. Saeki, S. Morishita, T. Asaoka, *J. Power Sources* **2013**, *238*, 53.

[131] S. Ohta, J. Sekim, Y. Yagi, Y. Kihira, T. Tani, T. Asaoka, *J. Power Source* **2014**, *265*, 40.

[132] F. Han, J. Yue, C. Chen, N. Zhao, X. Fan, Z. Ma, T. Gao, F. Wang, X. Guo, C. Wang, *Joule* **2018**, *2*, 497.

[133] T. Liu, Y. Ren, Y. Shen, S.-X. Zhao, Y. Lin, C.-W. Nan, *J. Power Sources* **2016**, *324*, 349.

[134] K. Sairam, J. K. Sonber, T. S. R. Ch. Murthy, C. Subramanian, R. K. Fotedar, P. Nanekar, R. C. Hubli, *Int. J. Refract. Met. Hard Mater.* **2014**, *42*, 185.

[135] R. Kali, A. Mukhopadhyay, *J. Power Sources* **2014**, *247*, 920.

[136] S. P. Woo, S. H. Lee, Y. S. Yoon, *Composites, Part B* **2017**, *124*, 242.

[137] R. Koerver, W. Zhang, L. D. Biasi, S. Schweidler, A. O. Kondrakov, S. Kolling, T. Brezesinski, P. Hartman, W. G. Zeier, J. Janek, *Energy Environ. Sci.* **2018**, *11*, 2142.

[138] L. D. Biasi, G. Lieser, C. Drager, S. Indris, J. Rana, G. Schumacher, R. Monig, H. Ehrenberg, J. R. Binder, H. GeBwein, *J. Power Sources* **2017**, *362*, 192.

[139] G. Bucci, T. Swamy, Y.-M. Chiang, W. C. Carter, *J. Mater. Chem. A* **2017**, *5*, 19422.

[140] G. Bucci, T. Swamy, Y.-M. Chiang, W. C. Carter, *J. Electrochem. Soc.* **2017**, *164*, A2660.

[141] D. Wang, Q. Sun, J. Luo, J. Liang, Y. Sun, R. Li, K. Adair, L. Zhang, R. Yang, S. Lu, H. Huang, X. Sun, *ACS Appl. Mater. Interfaces* **2019**, *11*, 4954.

[142] R. Koerver, I. Aygun, T. LeichtweiB, C. Dietrich, W. Zhang, J. O. Binder, P. Hartmann, W. G. Zeier, J. Janek, *Chem. Mater.* **2017**, *29*, 5574.

[143] T. Liu, Y. Zhang, R. Chen, S.-X. Zhao, Y. Lin, C.-W. Nan, Y. Shen, *Electrochem. Commun.* **2017**, *79*, 1.

Changbao Zhu is a Professor of Department of Materials Science and Engineering in Sun-Yat Sen University, China. He worked with Prof. Maier as a postdoc and received his doctoral degree in Max Planck Institute for solid state research, Germany. He graduated in France from the European master program "Materials for Energy Storage and Conversion." Prior to that, He obtained master degree in Xiamen University and bachelor degree in Chongqing University, China. His research interests focus on nanoionics and advanced energy storage systems, i.e., lithium (sodium) ion batteries and solid state batteries.

Xueliang Sun is a Canada Research Chair in Development of Nanomaterials for Clear Energy, Fellow of the Royal Society of Canada and Canadian Academy of Engineering and Full Professor at University of Western Ontario, Canada. He received his Ph.D. in materials chemistry in 1999 from University of Manchester, UK. Afterward he worked as a postdoctoral fellow at University of British Columbia, Canada and a research associate at L'Institue National de la Recherche Scientifique (INRS), Canada. His current research interests are focused on advanced materials for electrochemical energy storage and conversion, including electrocatalysis in fuel cells and electrodes in lithium-ion and metal–air batteries.

Yong Yang is a distinguished professor in chemistry in the State Key Lab for Physical Chemistry of Solid Surface at Xiamen University since 1997. He also serves as Editor for J Power Sources and Board Member of International Battery Materials Association (IBA) and International Meeting of Lithium Battery (IMLB). His main research interests are new electrode/electrolyte materials for Li/Na-ion batteries, in situ spectroscopic techniques, and interfacial/bulk reaction mechanism study in electrochemical energy storage and conversion system.